

The Open University's repository of research publications  
and other research outputs

## Martian atmospheric temperature and density profiles during the 1st year of NOMAD/TGO solar occultation measurements

### Journal Item

#### How to cite:

López Valverde, MiguelAngel; Funke, Bernd; Brines, Adrian; Stolzenbach, Aurélien; Modak, Ashimananda; Hill, Brittany; GonzálezGalindo, Francisco; Thomas, Ian; Trompet, Loic; Aoki, Shohei; Villanueva, Gerónimo; Liuzzi, Giuliano; Erwin, Justin; Grabowski, Udo; Forget, Francois; Lopez Moreno, José Juan; RodriguezGómez, Julio; Ristic, Bojan; Daerden, Frank; Bellucci, Giancarlo; Patel, Manish and Vandaele, AnnCarine (2022). Martian atmospheric temperature and density profiles during the 1st year of NOMAD/TGO solar occultation measurements. *Journal of Geophysical Research: Planets* (Early access).

For guidance on citations see [FAQs](#).

© [not recorded]



<https://creativecommons.org/licenses/by-nc-nd/4.0/>

Version: Accepted Manuscript

Link(s) to article on publisher's website:  
<http://dx.doi.org/doi:10.1029/2022je007278>

---

Copyright and Moral Rights for the articles on this site are retained by the individual authors and/or other copyright owners. For more information on Open Research Online's data [policy](#) on reuse of materials please consult the policies page.

---

# Martian atmospheric temperature and density profiles during the 1st year of NOMAD/TGO solar occultation measurements

Miguel-Angel López Valverde<sup>1</sup>, Bernd Funke<sup>1</sup>, Adrian Brines<sup>1</sup>, Aurélien Stolzenbach<sup>1</sup>, Ashimananda Modak<sup>1</sup>, Brittany Hill<sup>1</sup>, Francisco González-Galindo<sup>1</sup>, Ian Thomas<sup>3</sup>, Loic Trompet<sup>3</sup>, Shohei Aoki<sup>2</sup>, Gerónimo Villanueva<sup>7</sup>, Giuliano Liuzzi<sup>7,8</sup>, Justin Erwin<sup>3</sup>, Udo Grabowski<sup>9</sup>, Francois Forget<sup>10</sup>, José Juan Lopez Moreno<sup>1</sup>, Julio Rodriguez-Gómez<sup>1</sup>, Bojan Ristic<sup>3</sup>, Frank Daerden<sup>3</sup>, Giancarlo Bellucci<sup>11</sup>, Manish Patel<sup>12</sup>, Ann-Carine Vandaele<sup>3</sup>, and the NOMAD team

<sup>1</sup>Instituto de Astrofísica de Andalucía (IAA/CSIC), Granada, Spain

<sup>2</sup>Japan Aerospace Exploration Agency (JAXA), Japan

<sup>3</sup>Belgian Royal Institute for Space Aeronomy, Brussels, Belgium

<sup>6</sup>Space Science Institute, Boulder, USA

<sup>7</sup>NASA Goddard Space Flight Center, USA

<sup>8</sup>American University, Washington DC, USA

<sup>9</sup>Karlsruhe Institute of Technology, Institute of Meteorology and Climate Research, Karlsruhe, Germany

<sup>9</sup>Laboratoire de Meteorologie Dynamique, Paris, France

<sup>11</sup>Institute for Space Astrophysics and Planetology, Italy

<sup>12</sup>Open University, Milton Keynes, UK

## Key Points:

- Temperature and density profiles up to 90 km are retrieved from NOMAD 1st year of solar occultations, covering two seasons of MY34.
- NOMAD temperatures agree well with climate model predictions below 50 km but are wavier and globally colder by about 10 K at high altitudes.
- We report large thermal tides producing warm layers at 80 km in the morning terminator. Also strong warming by the 2018 global dust storm.

---

Corresponding author: M. A. López-Valverde, [valverde@iaa.es](mailto:valverde@iaa.es)

This article has been accepted for publication and undergone full peer review but has not been through the copyediting, typesetting, pagination and proofreading process, which may lead to differences between this version and the [Version of Record](#). Please cite this article as [doi: 10.1029/2022JE007278](https://doi.org/10.1029/2022JE007278).

This article is protected by copyright. All rights reserved.

## Abstract

We present vertical profiles of temperature and density from solar occultation (SO) observations by the “Nadir and Occultation for Mars Discovery” (NOMAD) spectrometer on board the Trace Gas Orbiter (TGO) during its first operational year, which covered the second half of Mars Year 34. We used calibrated transmittance spectra in 380 scans, and apply an in-house pre-processing to clean data systematics. Temperature and CO<sub>2</sub> profiles up to about 90 km, with consistent hydrostatic adjustment, are obtained, after adapting an Earth-tested retrieval scheme to Mars conditions. Both pre-processing and retrieval are discussed to illustrate their performance and robustness. Our results reveal the large impact of the MY34 Global Dust Storm (GDS), which warmed the atmosphere at all altitudes. The large GDS aerosols opacity limited the sounding of tropospheric layers. The retrieved temperatures agree well with global climate models (GCM) at tropospheric altitudes, but NOMAD mesospheric temperatures are wavier and globally colder by 10 K in the perihelion season, particularly during the GDS and its decay phase. We observe a warm layer around 80 km during the Southern Spring, especially in the Northern Hemisphere morning terminator, associated to large thermal tides, significantly stronger than in the GCM. Cold mesospheric pockets, close to CO<sub>2</sub> condensation temperatures, are more frequently observed than in the GCM. NOMAD CO<sub>2</sub> densities show oscillations upon a seasonal trend that track well the latitudinal variations expected. Results uncertainties and suggestions to improve future data re-analysis are briefly discussed.

## Plain Language Summary

The detailed variation of temperature and density with altitude is of paramount importance to characterize the atmospheric state and to constrain the chemistry and dynamics as a whole. The NOMAD instrument on board the Trace Gas Orbiter has among its key targets the characterization of the thermal state with unprecedented vertical resolution. This is the target of this work, where we analyzed transmittance spectra obtained from the NOMAD solar occultation channel, with a state-of-the-art retrieval scheme, adapted from Earth to Mars conditions and geometry. We applied it to the 1st year of TGO observations, which covered the last two Mars seasons of Mars Year 34. The results permit to study the temperature structure up to 90 km and its seasonal and latitudinal variations, revealing the impact of the MY34 Global Dust Storm, a warm layer at mesospheric altitudes not present in climate models, more frequent cold pockets than in current global climate models, and generally, colder temperature at those altitudes, all of which can be of importance for the validation of these climate models.

## 1 Introduction

The NOMAD and the Atmospheric Chemistry Suite (ACS) are the two key instruments on board the ExoMars 2016 Trace Gas Orbiter, primarily devoted to trace gas detection and mapping (Vandaele et al., 2018; Korablev et al., 2018). The solar occultation observational strategy of these two instruments offer excellent opportunities to sound up to very high in the atmosphere in unprecedented vertical resolution in order to perform unique science at mesospheric and thermospheric altitudes (López-Valverde et al., 2018). The thermal structure of an atmosphere is of pivotal importance to understand its radiation, dynamics and chemistry, all of which in turn affect such state. An excellent review of past observations of the atmospheric thermal state in Mars can be found in Smith et al. (2017). The precise characterization of the atmospheric structure is necessary to correctly interpret the search for trace species, and is also in itself one of the goals of the TGO mission, and of NOMAD in particular. For this reason, NOMAD performs routine observations in several spectral intervals

78 to achieve a good mapping of the atmospheric thermal state, and the analysis of these  
79 data is the primary goal of this work.

80 This work, together with other three companion manuscripts in this special issue,  
81 represent the first effort carried out in the IAA/CSIC within our scientific plan for the  
82 exploitation of both NOMAD and ACS datasets with a common analysis and retrieval  
83 strategy. This consists of using an state-of-the-art retrieval scheme, described below,  
84 to both instruments. Here we report its application to NOMAD solar occultation data,  
85 focused on the first year of the TGO science phase, from April 2018 to March 2019,  
86 which covers approximately two Mars seasons. These range from solar longitudes Ls  
87 160° to Ls 360°, i.e., the Southern spring and summer seasons, sometimes collectively  
88 names as the Martian perihelion period.

89 Following Smith et al. (2017), we will refer to the altitudes below about 50 km as  
90 troposphere or lower atmosphere and those above as mesosphere or middle atmosphere.  
91 We separate the mesosphere in lower and upper, as those regions below and above 90  
92 km respectively, the upper one extending up to the mesopause, around 120 km (López-  
93 Valverde et al., 2018). This work is devoted to the study of one of the diffraction orders  
94 in the NOMAD/SO channel, with in-house label # 149, which approximately covers  
95 the spectral interval 3349-3375 cm<sup>-1</sup>, and was used extensively in the NOMAD science  
96 team for the study of the thermal structure on Mars during its first year of operations.  
97 As we will show below, this SO order permits to sound up to 90 km altitude, i.e., our  
98 target regions in this work are the troposphere and the lower mesosphere of Mars.

99 There are two recent publications presenting temperature profiles from TGO  
100 solar occultation measurements by ACS. First, Fedorova et al. (2020) presented tem-  
101 peratures from the NIR channel during the first year of TGO science phase, which  
102 matches well the seasonal period and the altitude range covered in this work. Sec-  
103 ondly, Belyaev et al. (2021) presented profiles up to the mesopause, around 120 km,  
104 using a diffraction order containing H<sub>2</sub>O spectral lines, in a work devoted to H<sub>2</sub>O abun-  
105 dances at high altitudes. This second work presented temperatures in two consecutive  
106 perihelion seasons, for MY34 and MY35. The first one matches well the period studied  
107 here. We will make some comparisons with their results below.

108 The structure of the present work continues this Introduction with a section  
109 2 devoted to describe some relevant characteristics of the NOMAD/SO channel and  
110 the subset of measurements used in this work. Section 3 details the methodology  
111 and pipeline we used for these data analysis, pre-processing and inversion. Section  
112 4 presents the 3-D distribution of temperatures and densities obtained, and describe  
113 them to gain insight into atmospheric variability. Comparisons with previous works  
114 and with global climate model simulations are also presented there. Finally, Section 5  
115 presents a summary of the major results and plans to improve and extend this work  
116 to more NOMAD data, and also to ACS solar occultation data.

117 In addition to this work, other two manuscripts studying the thermal structure in  
118 solar occultation data from the TGO/NOMAD and ACS instruments have been sub-  
119 mitted to this issue. In the first one, Trompet et al. (2022) analyzed the NOMAD/SO  
120 channel's diffraction order 148 during Mars Years 35 and 36, excluding MY34 and  
121 focusing on mesospheric altitudes. The second presents profiles up to thermospheric  
122 altitudes combining two diffraction orders of the ACS/MIR channel, in a study cover-  
123 ing two full Martian years which is an extension of Belyaev et al. (2021). Each one of  
124 these works uses different inversion techniques and approximations, obtaining different  
125 retrieval errors and vertical resolutions. Our plan is to extend the present work to a  
126 larger dataset in the near future in order to perform a proper comparison with those  
127 two investigations.

## 128 2 NOMAD/SO measurements

### 129 2.1 NOMAD instrument

130 The NOMAD spectrometer, in routine operations since April 2018 on board the ExoMars  
131 2016 Trace Gas Orbiter, has 3 channels from the ultraviolet (UV) to the near-infrared  
132 (IR), each one with its own telescopic pointing and internal optics and detectors. NOMAD  
133 main scientific objectives include the search for trace species, the track of their sources and  
134 sinks, and the mapping of the thermal structure and the atmospheric composition at high  
135 sampling rate in the vertical, from the ground up to the thermosphere (Vandaele et al.,  
136 2018; López-Valverde et al., 2018). Its Solar Occultation channel (SO), in contrast to the  
137 other two channels, was designed for only solar occultation measurements and covers the  
138 range between 2.3 and 4.3  $\mu\text{m}$  (2320-4350  $\text{cm}^{-1}$ ) with a nominal resolving power close to  
139 20000 (Neefs et al., 2015). With a slit oriented quasi-perpendicular to the surface of the  
140 planet in the limb, the SO channel samples the atmosphere at one tangent altitude every  
141 second approximately. The SO detector's focal plane array is made up of 320 pixels along  
142 the spectral axis and 256 rows in the spatial direction, with 30  $\mu\text{m}$  x 30  $\mu\text{m}$  individual  
143 pixel sizes (Neefs et al., 2015). The SO slit is projected into 30 detector rows (a little larger  
144 than the Sun projected size) times 2 pixels wide. This represents a 1x12 km as projected  
145 onto the limb. Up to 6 diffraction orders of the echelle grating can be selected at a given  
146 altitude. From the downlink limitation that only 24 spectra can be transmitted to Earth  
147 per observation, this implies that only 4 spectra per order can be recorded (Vandaele et al.,  
148 2018). The usual SO operations combine pixels in the spatial dimension into four "detector  
149 bins", hence producing the required four spectra, each pointing to a slightly different tangent  
150 altitude. These detector bins, which can contain up to a maximum of 6 individual pixels,  
151 determine the instantaneous field-of-view (FOV), which is normally 2 x 4 arcmin, or about  
152 1x2 km at the limb. Depending on the  $\beta$ -angle (that between the TGO orbital plane and  
153 the solar direction), the number of altitudes sampled per scan can be very variable, but at  
154 least a few dozen points in the vertical are usually available. Together with the mentioned  
155 field-of-view, the SO channel allows to build vertical profiles with unprecedented resolution  
156 in every scan, twice per orbit. This channel contains an Acousto-Optical Tunable Filter  
157 (AOTF) which selects different spectral windows (with a width that varies from 20 to 35  
158  $\text{cm}^{-1}$ ). Routine operations are planned ahead of time with specific scientific goals in mind,  
159 i.e., with one particular combination of diffraction orders in each scan. More details on the  
160 original design, calibration and expected performance, and regular operations can be found  
161 in several publications (Vandaele et al., 2018; Thomas et al., 2016; Robert et al., 2016;  
162 Trompet et al., 2016; Liuzzi et al., 2018; Vandaele et al., 2019).

### 163 2.2 Dataset

164 NOMAD science operations began in April 2018, once the TGO spacecraft reached its final  
165 quasi-circular orbit, at about 400 km above the Martian surface, after a long aerobraking  
166 phase and a commissioning phase. In this work we selected data during the first year of routine  
167 operations in its science phase, from April 2018 until March 2019, which approximately  
168 covers the 2nd half of MY34: solar longitudes  $L_s = 160^\circ - 355^\circ$ . For the retrievals of  
169 temperature and density in this work we selected diffraction order 149 (3349-3375  $\text{cm}^{-1}$ )  
170 which was very frequently used during this first year of observations and contains CO<sub>2</sub> ro-  
171 vibrational lines of intermediate strength (see Figure 1). As we show below in section 4, this  
172 order permits a good sounding at tangent altitudes up to about 90 km. During the period  
173 selected, we used about 380 type-A scans (internal name for scans using that diffraction  
174 order at all altitudes during the solar occultation scan), spanning a diverse set of latitudes  
175 and solar longitudes, typical of the particular solar occultation mapping by TGO, as shown  
176 in Figure 1. There are stronger CO<sub>2</sub> ro-vibrational bands within the SO range than those  
177 mapped by diffraction order 149, in particular those in the 2.7  $\mu\text{m}$  region, dominated by  
178 the two fundamental bands of the major CO<sub>2</sub> isotope. These are captured by SO orders  
179 159-165 and are intended to sound up to thermospheric altitudes due to their much larger

180 optical thickness. We studied them in detail but found them to be very sensitive to error  
181 correlations at high altitudes and to the strong non-linear dependence of their absorption  
182 on temperature around the mesopause. We plan to tackle these bands in a near future after  
183 a better handling of the noise correlation and after a combination of adjacent orders; both  
184 of these extensions are within our ongoing improvements in the SO data analysis.

### 185 3 Data analysis

186 The NOMAD/SO data used in this work are Level 1A calibrated transmittance from the  
187 latest pipeline processing at the Belgian Institute for Space Aeronomy (IASB-BIRA,  
188 NOMAD's PI team) (Thomas et al., 2021). The inversion of temperature and density  
189 presented here is part of a broader effort at IAA/CSIC devoted to the scientific  
190 exploitation of NOMAD and ACS measurements with a common data analysis scheme.  
191 We followed a sequential retrieval strategy, starting with the inversion of atmospheric  
192 opacity from the continuum in the solar occultation data, then the temperature and  
193 density, and these are used later in the inversion of trace species (see the two companion  
194 papers on H<sub>2</sub>O and CO by Brines et al. (2022) and by Modak et al. (2022), respectively).  
195 At the core of the inversion scheme is a line-by-line radiative transfer Forward Model  
196 (KOPRA, see for example Stiller (2000)) and an inversion control program (or RCP in  
197 short, see von Clarmann et al. (2003)) originally developed at the University of Karlsruhe,  
198 and briefly described below in section 3.2. The calibrated transmittances are not yet  
199 suitable to be ingested by the retrieval suite but a very important cleaning or  
200 pre-processing is needed first. This is described next in some detail, as it affects not only  
201 this work but also the companion retrieval works.

#### 202 3.1 Data cleaning and pre-processing

203 The pre-processing phase of the data analysis at IAA is schematically shown in Figure 2  
204 and is devoted to correct for remaining imprecisions still present in the calibrated  
205 transmittances. These features include spectral shifts and residual spectral bending across  
206 the diffraction orders which can be quite significant in some spectra. These problems are  
207 common to all diffraction orders but different for each one of them and variable from scan  
208 to scan, as they depend on temperature effects on the detector, on TGO orbital conditions  
209 which in turn impact the space signals, and on drifts through time in the behavior of the  
210 grating's blaze response (Liuzzi et al., 2018; Thomas et al., 2021). These effects are shown  
211 for one specific scan in Figure 3.

212 Other effects, like the precise response of the AOTF and the NOMAD/SO line shape (ILS)  
213 also require analysis at this pre-processing level, as well as during the inversion of scientific  
214 data. Our effort devoted to the AOTF and ILS characterization aligns with parallel efforts  
215 by other teams in the NOMAD consortium and are described in a companion paper by  
216 Villanueva et al. (2022) in this special issue. In brief, we are using an asymmetric  
217 sinc-squared function for the AOTF whose center accounts for variations in detector  
218 temperature, and a double-Gaussian ILS with separation and ratio between the Gaussians  
219 which vary across each order and changing through the different SO diffraction orders.

220 An important defect in the spectra is the bending, which is very variable and can be very  
221 significant. It is particularly worrying for the precise determination of the actual  
222 atmospheric opacity. Fortunately its spectral shape can approximately be characterized  
223 (and corrected) by a simple polynomial fitting. However this correction is only  
224 approximate if the gas absorption lines are not taken into account. A more careful  
225 treatment is needed, especially for exploiting spectra at high tangent altitudes, where the  
226 absorption lines are weak and a simple bending correction of the full order can alter the  
227 baseline continuum and produce large biases.

Our pre-processing strategy essentially splits the measured transmittance in contributions along the ray path starting at the Sun and going through the atmosphere, first, and through the SO channel optics later. One of the possible characterizations of these contributions can be expressed as:

$$T_m = T_{GAS} \times T_{AEROSOLS} \times T_b \times R1_{NOISE}$$

where  $T_m$  is the measured transmittance,  $T_{GAS}$  is the atmospheric transmittance due to the target species (CO<sub>2</sub> in the case of temperature and density retrievals), and  $T_{AEROSOLS}$  is the absorption of the solar flux produced by the atmospheric aerosols along the Line of Sight (LOS), which is considered here as a contaminant component and is computed by the pre-processing from the continuum component in the spectra. The term  $T_b$  stands for the residual bending, to be computed and corrected for. Finally, the term  $R1_{NOISE}$  stands for a random Gaussian centered at 1 and with a standard deviation similar to the noise transmittance. For the correction we simply minimize the ratios  $1 - T_m/T_{SIMUL}$ , where we have combined into the term,  $T_{SIMUL}$ , the observed aerosol slant transmittances together with a large set of line-by-line forward model calculations carried out with KOPRA for the expected atmospheric state (extracted from a global climate model, as explained below). To avoid unstable results when the atmospheric plus aerosol transmittances are very low (at low tangent altitudes), the actual function to minimize is modified to  $1 - (1 + T_m)/(1 + T_{SIMUL})$ . This is applied to each tangent altitude in every scan. We found this method very robust and precise, using synthetic data, although it is time consuming due to the brute-force calculation required to generate all the  $T_{SIMUL}$ .

Once the bending is corrected, the residual spectral shifts across the order are computed and corrected, again from comparisons with the line-by-line simulations at each spectrum (or tangent altitude) during a scan. For practical reasons and in preparation for the retrievals, we perform this cleaning in a set of spectral micro-windows. As found by other teams, the residual spectral shift in a scan is usually at the level of 0.1-0.3 cm<sup>-1</sup>, and is not constant through the diffraction order but usually follows a linear variation, as shown in Figure 3. However, this shift is approximately constant with altitude, as far as the data are not very noisy or strongly contaminated by aerosol absorption. These conditions need to be taken into account to define the “meaningful” altitude range for a correct shift correction. Then each order in each scan is corrected in that altitude range, and the same correction is applied at all other altitudes.

### 3.2 Retrieval scheme

In Figure 2, RCP stands for Retrieval Control Program, and is a multi-parameter non-linear least squares fitting of measured and modeled spectra (von Clarmann et al., 2003). At the core of this processor is a state-of-the-art line-by-line radiative forward model named KOPRA (Karlsruhe Optimized Radiative transfer Algorithm,) described by (Stiller, 2000). Very well tested on Earth atmosphere remote sounding projects, Kopra integrates the RT equation along the observed LOS which is computed for an ellipsoidal planetary surface including consideration of refraction. KOPRA was recently adapted to limb emissions on Mars (Jiménez-Monferrer et al., 2021), and now it has been adapted to solar occultation data on Mars for the first time, and in particular to the NOMAD/SO channel with implementation of the asymmetric AOTF transfer function and the double Gaussian ILS.

Key inputs to RCP are the initial guess and *a priori* information of the quantities to be retrieved, as well as the NOMAD data, after the cleaning described above. The *a priori* temperature and density profiles are taken from a specific run of the Mars Global Climate Model developed at the Laboratoire de Météorologie Dynamique (LMD-MGCM) (Forget et al., 1999, 2009), using the recent implementations of the water cycles (Navarro et al., 2014) and the dust scenarios appropriate for MY34 (Montabone et al., 2015, 2020). For

273 each NOMAD/SO scan, a temperature and density profile was extracted from the model  
274 at the location (latitude, longitude) and time (local time and Ls) of a central point in the  
275 occultation (for a tangent altitude of 50 km).

276 RCP solves iteratively the inverse problem (Rodgers, 2000) until convergence is achieved.  
277 The calculation of the model spectra and Jacobians is performed with KOPRA, being  
278 called in each step of the iteration. For the temperature inversion, we perform a  
279 hydrostatic adjustment in each iteration, to account for the varying atmospheric state  
280 when the thermal structure is changed, and therefore to guarantee realistic results in the  
281 temperature/pressure structure. This hydrostatic adjustment assumes a reference pressure  
282 at the lowermost tangent altitude available, and that pressure value is taken from the *a*  
283 *priori* reference atmosphere. As we detail below, these tangent altitude and reference  
284 pressure are dependent on the aerosol loading along the line of sight.

285 Convergence is reached when the change of retrieval parameters with respect to the  
286 previous iteration produces improvements in the difference measured – simulated spectra  
287 until they are smaller than the measurement noise. The SO noise plays a central role in  
288 the inversion and deserves some explanation. The measurement covariance matrix is  
289 calculated from the noise-equivalent spectral radiance provided with the NOMAD level 1a  
290 calibrated data. Figure 4 shows the NOMAD measurement noise in one particular scan,  
291 typical of the calibration in this order 149. The noise function shown in the left-hand  
292 panel is projected into three planes for easier visualization. The projection on the  
293 wavenumber-noise plane is also shown in the right-hand panel as an alternative view, using  
294 arbitrary colors at each altitude. The noise transmittances in this right-hand panel show  
295 more clearly their strong spectral variations with increases toward the edge of the  
296 diffraction orders, where the sensitivity is lower due to the shape of the AOTF. They are  
297 also clear the variations with altitude, following the dependence on shot noise, i.e., on the  
298 solar flux received in the detector (Thomas et al., 2016). This variation is specially strong  
299 at tropospheric altitudes, when the solar radiation is strongly absorbed, either by gas  
300 species or by dust. An analysis of the vertical oscillations in the transmittances at high  
301 altitudes gives smaller values than these “nominal” ones. Such a calculation is shown with  
302 black dots in the right-hand panel of Figure 4. Comparing with the higher envelope, which  
303 is the measurement noise at high tangent altitudes, our estimate is lower by a factor 2, and  
304 this is very representative of most scans. This means that the actual random component  
305 in the nominal noise is smaller. This result is specific of order 149, and in all our  
306 temperature retrievals we reduced the nominal measurement error by such a factor 2.

307 We use a Tikhonov-type regularization optimized for each diffraction order. This is  
308 dependent on the measurement noise and was optimized, first by performing synthetic  
309 retrievals, and later by examination of a large set of actual retrievals. The value used in  
310 this work, common to all scans, varies with altitude, as the measurement noise and the  
311 line absorption changes with tangent altitude across each scan, and was selected as a  
312 compromise between error propagation and vertical resolution.

313 At the end of the inversion, temperatures, densities and also an adjustment of the  
314 atmospheric pressure is obtained. This last retrieval product, internally called  
315 “Line-Of-Sight in the altitude”, was originally intended to account for possible biases in  
316 satellite pointing. In our case this represents deviations from the nominal altitude  
317 registration which improve the best fit. For the radiative transfer calculations the  
318 atmosphere is divided into 1-km wide layers from the surface up to 60 km, 2.0 km width  
319 layers from 60 to 90 km, 2.5 km-wide layers at 90-130 km and 5 km wide layers above.  
320 The output retrieved vectors also share this grid, which is common to all the IAA  
321 retrievals using NOMAD data and presented in this special issue.

322 Outside the SO measurement altitude range, we impose a strong regularization constraint,  
323 to give a large weight to the *a priori* information (to its vertical gradient, which will be  
324 imposed on the data). For the CO<sub>2</sub> density, a strong diagonalization at all altitudes below



80 km is used, for stability reasons, which effectively assumes the volume mixing ratio (VMR) in the *a priori* value is correct. It is well known that the CO<sub>2</sub> VMR is close to one up to the homopause, surely above the altitude range studied here. However, the CO<sub>2</sub> absolute density will be variable and determined from the NOMAD data via the hydrostatic inversion mentioned above, consistently with the thermal structure.

At low altitudes we avoid large dust contamination by filtering observations where the aerosol opacity is greater than a given value. For order 149 we use a maximum slant opacity of 2.0. Also we avoid steep gradients in the aerosol slant opacity, larger than 0.08 km<sup>-1</sup>.

The instrument transfer function of an AOTF (nominally a sinc-square) leads to the mixing of different echelle diffraction orders into the central one. Details of this effect in the case of NOMAD have been discussed previously (Mahieux et al., 2015; Liuzzi et al., 2018; Thomas et al., 2021). Following these guidelines and our own tests, we are accounting for the flux contribution of +/- 4 adjacent orders around the 149 (i.e. orders 145 to 143). Contributions beyond these orders are very small, well below 5%. However, the contribution from orders 148 and 150 are significant (between 10-30 % at some wavelengths) and we found that the fitting of these other orders' absorption lines is normally difficult, even after a careful fine tuning of the AOTF for this specific order. A practical solution adopted in this work is to use a powerful feature in RCP, namely, the use of internal spectral micro-windows instead of the full spectral range of the diffraction order. With the use of micro-windows we can select portions of the spectrum which are particularly valuable in terms of information content, and at the same time, omit very contaminated spectral segments. After extensive experimentation we adopted a set of 7 micro-windows for order 149, of diverse spectral widths, mostly located in the central part of the order to avoid the noisier edges, and which contain some of the strongest CO<sub>2</sub> lines in the order. They are shown with color horizontal bars in Figure 3. The pre-processing/cleaning is focused on the central part of the diffraction order, the region covered by the microwindows; this is why we obscured the outer spectral regions in Figure 3.

Figures 5 and 7 show the performance of the temperature inversion in one specific scan, *20180620\_0240338\_1p0a\_SO\_A\_I*, obtained on June 20th, 2018, for Ls 196° and at 55° N latitude, where a heavy dust loading was found below about 20 km. The Averaging Kernels in Figure 5 show a lack of information in this order above 95 km. Averaging Kernels matrices are very useful as diagnostics of the performance of the retrieval, and are standard outputs of our inversion code RCP. For example inspection of this matrix's rows illustrate the vertical resolution while its columns quantify the response to changes in the true state vector. Also the trace of this matrix gives the independent pieces of information, i.e., the degrees of freedom, which in the case of the scan in Figure 5 is 19. For its calculation RCP makes use of Jacobians computed/updated in every time step of the inversion, taking into account all the spectral information present in the selected microwindows. Figure 5 shows that the retrieval errors usually increase with altitude, in this scan from about 2 K at 20 km to about 5 K around 90 km. The vertical resolution, given by the width of the Averaging Kernel rows, also vary significantly with tangent altitude, between 3 km in the lowermost tangent altitude up to 10 km at the top range in this scan. The best-fit spectra at the end of the inversion usually reproduces the NOMAD data very well. Figure 7 shows the best fit obtained for this scan at about 65 km altitude, where the retrieved temperature significantly differs from the *a priori*. Sometimes high altitude spectra go slightly above Transmittance=1; these defects in the data are accounted for during the inversion by a simultaneous retrieval of the continuum at each altitude, which also includes a small shift in the continuum, as required for matching the data. To illustrate the robustness of the inversion against changes in the *a priori*, we show in Figure 6 the temperature inversion of another scan, *20180423\_204351\_1p0a\_SO\_A\_I*, obtained at 65° S latitude and Ls 164°, arbitrarily selected among the dataset. We

378 performed two retrievals, one using the nominal *a priori* GCM atmosphere and the other  
379 with an *a priori* profile arbitrarily increased by 30 K at all altitudes. As shown in Figure 6,  
380 the retrieved temperature is basically the same in both runs up to 80 km; above this  
381 altitude the relatively large measurement noise decreases the information content and  
382 starts pulling the retrieved profile towards the assumed climatology.

## 383 4 Results and discussion

384 The retrieval strategy discussed above was applied to our selection of 380 NOMAD/SO  
385 scans observed during MY34, as mentioned above. The convergence rate was high, with a  
386 final 338 retrieved temperature and CO<sub>2</sub> density profiles. We describe and discuss here the  
387 main results obtained.

388 We only show here results with a significant amount of information directly derived from  
389 the data. In the lowermost tangent altitudes and above about 95 km we apply a condition  
390 on the diagonal of the Averaging Kernels, to filter values only above 0.03. Lower values are  
391 considered as too biased towards *a priori*/climatological values, due to very low depth of  
392 the absorption lines at high altitudes and to aerosol contamination at low tangent  
393 altitudes.

### 394 4.1 Global envelope of atmospheric temperatures

395 Figure 8 shows all the temperature profiles retrieved in this work, put together in a single  
396 panel, with a similar plot for the LMD GCM profiles (our *a priori*). The dashed lines in  
397 blue and orange represent the envelope of all possible temperatures anywhere and anytime  
398 on Mars, taken from Smith et al. (2017), who compiled data from instruments Mars  
399 Climate Sounder and Thermal Emission Spectrometer, as well as from the Mars Climate  
400 Database simulations for extreme conditions.

401 The range of temperatures observed by NOMAD are quite similar to the GCM, although  
402 generally colder in the mesosphere. The global difference between 0.01 and 0.001 mb  
403 pressure levels (about 60-80 km altitude) seems to be over 10 K. In addition, and although  
404 possibly difficult to see in this Figure, the NOMAD temperatures seem to be wavier than  
405 in the GCM, and in particular we obtained excursions to very low temperatures at  
406 altitudes above 0.001 mb. At these altitudes, NOMAD temperatures reach values very  
407 close to the CO<sub>2</sub> condensation temperature, much closer than in the GCM.

### 408 4.2 Global Distribution of Temperatures

409 Figure 9 shows the global distribution of all the temperatures obtained, split in two  
410 hemispheres for clarity, and covering the second part of MY34. Some gaps in the maps  
411 correspond to lack of solar occultation data as the TGO-Sun  $\beta$ -angle becomes too large.  
412 Given the peculiar TGO solar acquisition sequence, the latitudes and seasons are linked  
413 and this needs to be taken into account when inspecting the maps.

414 The vertical thermal structure generally presents what can be considered as a typical  
415 Martian pattern in the vertical, with the usual two broad thermal layers, a warmer  
416 troposphere and a colder mesosphere, except near polar regions where the thermal regime  
417 can be quite different (Smith et al., 2017). This follows the warming at low altitudes by  
418 convection from the surface and the local heating by solar absorption by airborne dust. On  
419 the other hand, the atmospheric radiative cooling to space by diverse CO<sub>2</sub> ro-vibrational  
420 bands becomes an important term of the energy budget as we move upwards to the  
421 mesosphere, where these bands become optically thinner. There is a significant variability  
422 upon this generic profile, depending on diverse parameters (surface temperatures and dust  
423 amounts, together with other energy budget terms including dynamics), all of which vary  
424 along the TGO track, as latitude and seasons change across the X-axis in Figure 9.

### 4.3 MY34 Global Dust Storm

Several interesting features are observed in Figure 9, and the most prominent one is the strong warming period between Ls 190° and 220°, at all altitudes and in both hemispheres. This corresponds to the onset of the MY34 Global Dust Storm (GDS), which peaked around Ls 195°-205° (Montabone et al., 2020). As it is well known, the absorption of solar radiation by the dust particles, especially as they reach high altitudes, can be very efficient (Wolff et al., 2017). In this period the slant aerosol opacity is so large that the limb sounding using molecular spectral lines in this spectral region is impossible at tangent altitudes below 40 km, or even 55 km in some scans. We observe warm temperatures around 180 K up to 80-90 km altitude in the peak of the GDS, and tropospheric temperatures above 200 K up to 50 km.

The decay of the GDS seems apparent in Figure 9 by the progressive cooling at mesospheric altitudes from Ls 220° to 240° in the Northern Hemisphere (NH) at mid latitudes. This is more difficult to see in the Southern Hemisphere (SH) as this period follows large changes in TGO latitude coverage as well. In fact, there seem to be several warming periods at mesospheric altitudes in the SH, around Ls 220°, 260°, 285°, 315° and 340°, which coincide with the mapping of high latitudes in the SH. This seems to show a latitudinal gradient with warmer mesospheric temperatures at high latitudes during the whole perihelion season.

### 4.4 Global Distribution of atmospheric density

Similarly to Figure 9, Figure 10 shows the global distribution of all the CO<sub>2</sub> densities obtained. The strong exponential decrease in density with altitude seems to minimize other variations, with lower amplitudes, even using a log scale. Hence, in order to highlight these, we selected an altitude of 70 km and plotted in the two lower panels its variability with time, together with the GCM variability at that altitude. There are clear variations associated with the latitudinal change at the tangent point. For example, the three largest excursions in density, at Ls 355° in the NH and at Ls 170° and Ls 200° in the SH, are clearly associated to sudden changes in latitude in a short Ls period. In both hemispheres the sign of the response is similar: as the orbit approaches lower latitudes the density increases, following the warmer troposphere at low latitudes. Averaging over these variations one would expect to discern a seasonal trend with a maximum around the summer in the SH, around Ls 270°, when the atmospheric density in Mars presents a maximum (Smith et al., 2017). However, in Figure 10 the maximum is observed around Ls 200°, as a response to the MY34 GDS.

This analysis is complementary and agrees with a similar analysis by Trompet et al. (2022) in a companion paper in this special issue, who studied the variation of the atmospheric density in NOMAD retrievals for MY35. In the absence of GDS, the MY35 presents a maximum around Ls 270° in their work. Also the absolute values of the densities at 70 km agree well between both retrieval teams.

### 4.5 Corrections for the reference pressure

During the temperature and density retrieval, our inversion processor finds whether a change in the line-of-sight pointing, or in other words, in the tangent altitudes, would produce a better model-data fit than with the nominal pointing. Usually the correction found is small but without this correction the temperature profiles would be incorrectly positioned. The variation, expressed in km at the tangent point, is shown in Figure 11. Some profiles should be moved up and some down, with a globally averaged negative value around 2 km. Figure 11 also shows the absolute value of this correction.

The interpretation of this result is related to the assumed pressure reference for the hydrostatic adjustment. Pressure values from the GCM are taken at a given altitude, and

474 a hydrostatic atmosphere is built with this assumption. The results shown in Figure 11  
475 inform us that such an altitude seems to be wrong by a few km, according to NOMAD  
476 data. The envelope of the data points in the right-hand panel in this figure shows lower  
477 values at lower altitudes. This is suggesting that the pressure-altitude relationship is more  
478 correct in the GCM the lower we look in the atmosphere. This is not surprising, as the  
479 atmospheric variability should create differences with the GCM climatological state which  
480 increase with altitude.

#### 481 4.6 Latitudinal Variations

482 During MY34 there are two seasonal periods, around Ls 180° and Ls 290°, where the TGO  
483 mapping covers a wide range of latitudes in a short Ls interval. These offer a good  
484 opportunity to observe and characterize the latitudinal variations in temperature. We  
485 have grouped the scans in these periods exactly in boxes Ls=160°-190° and 285°-305° and  
486 show them in Figure 12, where they are compared to the same sampling and boxing in the  
487 GCM data (our *a priori*). Unfortunately, the numerous gaps in the data make it difficult  
488 to do a fine comparison on a pure altitude/latitude cross section map, but still some  
489 interesting results are clearly present.

490 For example, the NOMAD data in Ls Box #1 (left panels) seem to show a warm layer  
491 around 50 km around latitudes 60°N and 60°S, which is also seen in the GCM model and  
492 at similar altitudes. This agrees with the expected global description of the atmospheric  
493 temperatures in equinox conditions (seen in the bottom panels of Figure 12), in spite of  
494 the difference data-model (NOMAD temperature being generally colder than GCM at  
495 mesospheric altitudes). These warm layer is not seen in Ls Box #2 (right panels).

496 Another result which agree with the GCM simulations is the warm layer at the bottom of  
497 the observed altitudes in Ls Box #2 (right panels). These layers seem to correspond to the  
498 warming at high latitudes of the SH, typical of the Southern Summer solstice. These warm  
499 layers are absent in both model and data in the Ls Box #1 (left panels).

500 The latitudinal variations in the NOMAD temperatures seem to agree in these two periods  
501 with typical equinox and solstice conditions as simulated by the LMD-GCM.

#### 502 4.7 Local time variations

503 Inspection of the orbit in Figures 1 or 8 reveals a couple of periods with a significant  
504 variation in local time in a short Ls period and small variations in latitude as well. These  
505 two periods are analyzed here in the search for possible variations with local time. Period  
506 “CT Box1” covers latitudes 20°-50° in the NH during the bracket Ls 230°-250°, and  
507 period “CT Box2” covers latitudes 30°N-60°N and Ls 290°-310°. We grouped all the scans  
508 inside these boxes splitting them by their local time only, and are shown in Figure 13. The  
509 figure also shows the LMD GCM profiles for the same scans.

510 In CT Box1 there are no significant differences between the morning and evening results,  
511 neither in the NOMAD data nor in the model, although the NOMAD data shows a colder  
512 layer at 60 km altitude within a more wavy vertical profile. CT Box2 shows also a more  
513 wavy profile in NOMAD than in the model, with a possibly upward propagating wave with  
514 large amplitudes, around 30 K in the mesosphere, which is much weaker in the GCM. This  
515 oscillation seems to be smaller in the NOMAD evening profiles, although there are not  
516 many profiles to examine and one of them also presents a large oscillation. The warm layer  
517 at 80 km in the NOMAD morning data could be related to the recent finding of a warm  
518 layer at precisely that altitude at nighttime in stellar occultation data from IUVS/Maven  
519 (Nakagawa et al., 2020).

520 A similar warm layer was reported also by (Belyaev et al., 2021) using ACS solar  
521 occultation data in the ACS/MIR channel. The data used by (Belyaev et al., 2021) are

not exactly collocated with NOMAD observations. In their retrievals the warm layer was found as more localized around  $L_s 270^\circ$ , and present in both MY34 and MY35 but only in the NH. Although not discussed by them, their results combined with ours indicate a peculiar period of time around perihelion, at the end of the Southern summer where thermal tides at mid latitudes seem to present very strong amplitudes, greatly affecting the lower mesosphere. It will be interesting to extend the current study to cover more Martian years, and also to compare more quantitatively with ACS/MIR results, in order to confirm this strong thermal tide and to analyze its year-to-year variability with the good vertical resolution of these two instruments on board TGO.

Upward propagation of waves has been recently studied by (Starichenko et al., 2021) but this work was very focused on gravity waves and small scale structures observed in the ACS/MIR temperature vertical profiles, not on the thermal tides.

#### 4.8 Latitudinal-Seasonal slices at fixed altitudes

Figure 14 shows the structure of the NOMAD temperatures in latitude - solar longitude cross sections at three altitudes, 30, 50 and 80 km, compared with the *a priori* GCM temperatures. Again we observe a NOMAD thermal field colder than the GCM at mesospheric altitudes and a better agreement in the troposphere. In this figure, and in spite of variability and differences, we observe that the 3-D map of NOMAD temperatures globally agree with the global thermal distribution simulated by the GCM for MY34. We observe a warm troposphere at 30 km at all latitudes during the GDS with a gradual cooling with time, in both data and model (left panels). At 50 km the warm layers are located at mid latitudes in both model and data but NOMAD does not see the warm branch at  $60^\circ\text{N}$  that the model simulated for the rest of MY34. It will be interesting to explore these comparisons in other Mars Years.

#### 4.9 Comparison with ACS/NIR temperatures

Temperature profiles from ACS/NIR have been reported by Fedorova et al. (2020) for a period of time similar to that covered in this work. Although a proper comparison campaign is beyond the scope of this manuscript, we have performed a first comparative study of a few dozens of profiles. We first looked for close coincidences to each of our NOMAD/SO retrieved profiles, defined as being observed by ACS/NIR on the same day, as determined by the solar longitude  $L_s$ , and within a small bracket in latitude, longitude and local time:  $\Delta LAT < 3^\circ$ ,  $\Delta LON < 20^\circ$  and  $\Delta LCT = 0.5$  hour. Only six coincidences were found, and they are shown in Figure 15. The agreement between both instruments is quite good, and in four of the six profiles the differences are approximately within their error brackets. The altitude range sampled by both instruments is very similar in all the profiles. At the top of the altitude range, at and above 90 km, the ACS/NIR retrieval errors increase a lot and also in our NOMAD/SO data the *a priori* effect starts to be significant. At the bottom of the profiles, both retrievals are limited by the aerosol absorption along the LOS, in approximately the same manner. Some of the features observed in the thermal profiles indicate that the vertical resolution in both instruments is also similar.

The number of coincidences between NOMAD/SO and ACS/NIR increases significantly when the criterion for geographical collocation is relaxed. In particular, with a relaxation in longitude to  $\Delta LON < 30^\circ$  we allow for profiles from adjacent orbits and then we found 95 coincidences. All these, which include the previous 6 closest ones, are shown in the Appendix, using a similar format to Figure 15. In general, considering the different retrieval methods and instrument characteristics, and the likely effect of a  $30^\circ$  shift in longitude, we consider the agreement as satisfactory. We observed many good matches, but also some significant discrepancies; we show examples of these two subsets in Figures 16 and 17.

571 Figure 16 shows a dozen of profiles with a good agreement between NOMAD/SO and  
572 ACS/NIR and which also present significant deviations from the *a priori*. The agreement  
573 is good except at the very top altitudes and at the bottom of the profiles, where noise and  
574 aerosols limit the sounding, respectively. Considering the different retrieval methods,  
575 instrument performances and spectral ranges used in our work and in Fedorova et al.  
576 (2020), these 12 profiles can be considered as robust determinations of the atmospheric  
577 state, and may be particularly valuable for GCM validation purposes. The largest  
578 discrepancies are found at mesospheric altitudes, and they present much colder  
579 temperatures than in the GCM, but also in some profiles there are discrepancies with the  
580 *a priori* below 50 km, like NOMAD/SO profiles #45, 81, 182, and 224 (see numbers in  
581 bracket in Figure 16). It would be interesting to extend the retrievals of both instruments  
582 to a couple of Mars years, in search for more significant deviations from the GCM  
583 climatological predictions.

584 Figure 17 shows a selection of another dozen profiles but in this case with clear differences  
585 between NOMAD/SO and ACS/NIR. As in the case of Figure 16, the separation between  
586 the "coincident" profiles is about 30°, which as said above, may play a role and partly  
587 explain some of the differences. The discrepancies are particularly large at mesospheric  
588 altitudes, and in general the NOMAD/SO profiles seem to be colder than the ACS/NIR at  
589 those altitudes. Again, it will be useful to explore more differences with ACS/NIR in the  
590 future, when both instruments' retrieval schemes are applied to a more extended dataset  
591 including a couple of full Martian years.

## 592 5 Conclusions

593 We present in this work the results of vertical profiles of temperature and CO<sub>2</sub> density  
594 from solar occultation observations by the NOMAD/SO channel in its diffraction order  
595 149 during the first year of TGO science operations.

596 For this purpose we adapted a well tested inversion scheme on Earth limb sounding  
597 experiments to solar occultation data on Mars for the first time. This scheme is used in a  
598 sequential manner to retrieve diverse targets from the NOMAD/SO data. Results on  
599 aerosol opacity's and physical properties, and on H<sub>2</sub>O and CO abundance profiles are  
600 presented in companion papers in this special issue. The analysis starts with a  
601 pre-processing phase, which permits to clear the SO calibrated transmittance of remaining  
602 issues like spectral shifts and bendings. This is followed by the actual retrieval, following  
603 an iterative application of a precise forward model, which uses micro-windows to eliminate  
604 severe contamination from adjacent diffraction orders, and solves temperature and density  
605 consistently, with incorporation of hydrostatic adjustments in each iteration. The inversion  
606 achieves best-fits with a high degree of convergence in the dataset analyzed here. The  
607 scheme is robust against *a priori* assumptions and permits meaningful retrievals typically  
608 up to about 90 km altitude.

609 The atmospheric thermal structure during the two Mars seasons in MY34 (the Martian  
610 perihelion half-year period) is characterized by the strong MY34 GDS episode, a well  
611 documented event peaking around Ls 195°-210° (Guzewich et al., 2019; Montabone et al.,  
612 2020). Our results show that the GDS warmed the atmosphere significantly at all sounded  
613 altitudes, with episodes where 180 K are observed at 80 km altitude in the NH and up to  
614 100 km in the SH. The thermal impact is clearly observed during an extended decay phase  
615 up to about Ls 250°. During this period the retrievals are difficult in the troposphere due  
616 to the strong dust opacity. The impact of the regional dust storm (GDS) around Ls 330°,  
617 near the end of the period studied in this work, is less clear in our data. This can be due  
618 to several reasons. The first one is the lower amount of aerosols injected into the  
619 atmosphere by the regional storm. A second possible reason is the limited sampling in  
620 space and time that solar occultations have from the TGO orbit; this mapping may have  
621 skipped the peak activity of this RDS.

622 Regarding the comparison of the retrieved thermal structure with the LMD Mars GCM  
623 simulations used here as *a priori*, the NOMAD temperatures are in good agreement at  
624 tropospheric altitudes but are generally wavier and colder at mesospheric altitudes. The  
625 atmospheric oscillations reach values close to the CO<sub>2</sub> condensation temperature at  
626 mesospheric altitudes much more frequently than in the GCM. This may be explained by a  
627 stronger atmospheric tidal activity than in the model, particularly during the GDS peak  
628 and decay phases, but also elsewhere through the perihelion season. In particular, a warm  
629 layer around 80 km is found in the morning terminator in the NH during Ls 260°-300°,  
630 which is clearly absent in the GCM. A warm layer is also observed in the evening  
631 terminator but more sporadically. These two global results, a colder mesosphere and a  
632 warm layer around 80 km were also found very recently by Belyaev et al. (2021).

633 Regarding the latitudinal and local time variations, our data is patchy and the TGO  
634 orbital mapping does not allow us to build pure latitude or pure local time cross sections.  
635 Instead, some boxing is required, which are not free from a mixture of effects. However,  
636 with the help of scan-to-scan comparisons with the GCM and of global maps created with  
637 the GCM specifically for this comparisons, it seems that our NOMAD retrievals do track  
638 the expected thermal structure typical of equinoxes and solstices during the observed  
639 period. The main conclusions regarding local time variations is the clearly stronger tidal  
640 activity in the morning terminator, mentioned above.

641 A second retrieval product is the atmospheric CO<sub>2</sub> density, whose global distribution  
642 shows very clear latitudinal effects, especially when looking at a single altitude, like 70 km.  
643 On top of these, a seasonal trend seems also present, although the occurrence of the GDS  
644 in the early Southern Spring dominates the seasonal pattern and hides the expected  
645 maximum around Ls 270° that should be typical of non-GDS Mars years. It will be very  
646 interesting to revisit this when an extended SO dataset covering several MY are processed.

647 Another interesting product of our retrieval scheme is the so called “LOS correction”,  
648 which permits to revisit the hydrostatic assumption, based on using a given pressure level  
649 at a given altitude, usually taken from the climatology or *a priori* dataset. In our case, the  
650 correction indicates that the LMD MGCM pressures at the lowermost tangent altitude of  
651 our retrieval range are globally correct, except for a small correction of a couple of km.  
652 This agreement is better in dust-clear conditions, when our sounding can be extended to  
653 the lower troposphere, below 20 km. Below this altitude, the lower the sounding, the  
654 smaller the correction. In some scans the altitude adjustment to reconcile NOMAD and  
655 GCM can reach up to 10 km.

656 We plan to continue the analysis of NOMAD/SO data by extending our retrieval scheme to  
657 the whole SO dataset available to date, covering two full Mars Years. A few issues remain  
658 to be improved also and we plan to tackle them, in a joint effort with other NOMAD  
659 teams. These include a better characterization of the SO measurement noise in order to  
660 eliminate remaining systematics, and the combination of two different SO orders. For  
661 example, the combination of orders 149 and 165, this one with much stronger absorption  
662 lines from the CO<sub>2</sub> 2.7- $\mu$ m fundamental band, should help to extend the retrieval range  
663 from 90 km up to 160 or 170 km. In addition, the application of our retrieval scheme to the  
664 ACS/MIR data is an ongoing task in our team at IAA/CSIC. The results and comparisons  
665 between NOMAD/SO and ACS/MIR during a full Mars year will be presented elsewhere.

## 666 **Appendix A Sample of 95 near coincidences between NOMAD/SO and** 667 **ACS/NIR**

668 As explained in section 4.9, we performed a comparison of our NOMAD/SO temperature  
669 retrievals with the ACS/NIR thermal profiles reported by Fedorova et al. (2020), which  
670 approximately extend over the last half of MY34. A total of 95 “near coincidences” are  
671 found when using the following selecting criteria in solar longitude, latitude, longitude and

672 local time:  $\Delta Ls < 0.1^\circ$ ,  $\Delta LAT < 5^\circ$ ,  $\Delta LON < 30^\circ$  and  $\Delta LCT = 0.5$  hour. The 95  
673 comparisons are shown in Figures A1 to A8, split in 8 subsets of a dozen profiles each.  
674 Notice that these figures contain the comparisons already shown in Figures 15, 16 and 17  
675 above.

## 685 Acknowledgments

686 The IAA/CSIC team acknowledges financial support from the State Agency for Research  
687 of the Spanish MCI through the ‘Center of Excellence Severo Ochoa’ award for the  
688 Instituto de Astrofísica de Andalucía (DEV-2017-0709) and funding by grants  
689 PGC2018-101836-B-I00 (MCI/AEI/FEDER, EU),  
690 PID2019-110689RB-I00/AEI/10.13039/501100011033, and RTI2018-100920-J-I00.  
691 ExoMars is a space mission of the European Space Agency (ESA) and Roscosmos. The  
692 NOMAD experiment is led by the Royal Belgian Institute for Space Aeronomy  
693 (IASB-BIRA), assisted by Co-PI teams from Spain (IAA-CSIC), Italy (IN AF-IA PS), and  
694 the United Kingdom (Open University). This project acknowledges funding by the Belgian  
695 Science Policy Office (BELLS), with the financial and contractual coordination by the  
696 ESAU Prod ex Office (PEA 4000103401, 4000121493) as well as by UK Space Agency  
697 through grants ST/V002295/1, ST/V005332/1 and ST/S00145X/1 and Italian Space  
698 Agency through grant 2018-2-HHS.0. US investigators were supported by the National  
699 Aeronautics and Space Administration. This work was supported by the Belgian Funds de  
700 la Recherche Scientific – FIRS under grant number 30442502 (ET\_HOME). This project  
701 has received funding from the European Union Horizon 2020 research and innovation  
702 program under grant agreement No 101004052 (Road Map project). We want to thank the  
703 LMD and LATMOS teams for the continuous development of the LMD-MGCM.

## 704 Open Research/ Data availability

705 The NOMAD-SO Level 1a calibrated transmittance data used in this work are available at  
706 the European Space Agency (ESA) planetary archive (<https://archives.esac.esa.int/psa>),  
707 and also at the NOMAD data center (<https://nomad.aeronomie.be/index.php/data>,  
708 (Thomas et al., 2021), (Vandaele et al., 2019)).  
709 The results retrieved from the NOMAD measurements presented in this article are being  
710 archived and available from (López-Valverde, 2022).

## 711 References

712 Belyaev, D. A., Fedorova, A. A., Trokhimovskiy, A., Alday, J., Montmessin, F., Korablev,  
713 O. I., ... Shakun, A. V. (2021). Revealing a high water abundance in the upper  
714 mesosphere of mars with acs onboard tgo. *Geophysical Research Letters*, 48(10),



- 715 e2021GL093411. Retrieved from  
 716 <https://agupubs.onlinelibrary.wiley.com/doi/abs/10.1029/2021GL093411>  
 717 (e2021GL093411 2021GL093411) doi: <https://doi.org/10.1029/2021GL093411>
- 718 Brines, A., López-Valverde, M. A., Stolzenbach, A., Modak, A., Funke, B.,  
 719 Gonzalez-Galindo, F., ... the NOMAD Team (2022). Water vapor vertical  
 720 distribution on mars during the perihelion season of MY34 and MY35 from  
 721 ExoMars-TGO/NOMAD solar occultation measurements. *JGR-submitted*.
- 722 Fedorova, A. A., Montmessin, F., Korablev, O., Luginin, M., Trokhimovskiy, A., Belyaev,  
 723 D. A., ... Wilson, C. F. (2020). Stormy water on mars: The distribution and  
 724 saturation of atmospheric water during the dusty season. *Science*, *367*(6475),  
 725 297–300. Retrieved from  
 726 <https://science.sciencemag.org/content/367/6475/297> doi:  
 727 10.1126/science.aay9522
- 728 Forget, F., Hourdin, F., Fournier, R., Hourdin, C., Talagrand, O., Collins, M., ... Huot.,  
 729 J.-P. (1999). Improved general circulation models of the Martian atmosphere from  
 730 the surface to above 80 km. *J. Geophys. Res.*, *104*, 24,155-24,176.
- 731 Forget, F., Montmessin, F., Bertaux, J.-L., González-Galindo, F., Lebonnois, S.,  
 732 Quémerais, E., ... López-Valverde, M. a. (2009, January). Density and temperatures  
 733 of the upper Martian atmosphere measured by stellar occultations with Mars  
 734 Express SPICAM. *Journal of Geophysical Research*, *114*(E1), E01004. Retrieved  
 735 from <http://doi.wiley.com/10.1029/2008JE003086> doi: 10.1029/2008JE003086
- 736 Guzewich, S. D., Lemmon, M., Smith, C. L., Martinez, G., de Vicente-Retortillo, A.,  
 737 Newman, C. E., ... Zorzano Mier, M.-P. (2019). Mars science laboratory  
 738 observations of the 2018/mars year 34 global dust storm. *Geophysical Research*  
 739 *Letters*, *46*(1), 71-79. Retrieved from  
 740 <https://agupubs.onlinelibrary.wiley.com/doi/abs/10.1029/2018GL080839>  
 741 doi: <https://doi.org/10.1029/2018GL080839>
- 742 Jiménez-Monferrer, S., López-Valverde, M. A., Funke, B., González-Galindo, F., Piccialli,  
 743 A., García-Comas, M., ... Bibring, J.-P. (2021). Co2 retrievals in the mars daylight  
 744 thermosphere from its 4.3 $\mu$ m limb emission measured by omega/mex. *Icarus*, *353*,  
 745 113830. Retrieved from <hdl.handle.net/10261/220681> doi:  
 746 10.1016/j.icarus.2020.113830
- 747 Korablev, O., Montmessin, F., Trokhimovskiy, A., A.-A, Fedorova, Shakun, A.-V., ...  
 748 Zorzano, M.-P. (2018, Feb 30). The atmospheric chemistry suite (acs) of three  
 749 spectrometers for the exomars 2016 trace gas orbiter. *Space Sci. Rev.*, *214*(1), 62.  
 750 Retrieved from <https://doi.org/10.1007/s11214-017-0437-6> doi:  
 751 10.1007/s11214-017-0437-6
- 752 Liuzzi, G., Villanueva, G., J. Mumma, M., D. Smith, M., Daerden, F., Ristic, B., ...  
 753 Bellucci, G. (2018, 09). Methane on mars: New insights into the sensitivity of ch4  
 754 with the nomad/exomars spectrometer through its first in-flight calibration. *Icarus*,  
 755 *321*. doi: 10.1016/j.icarus.2018.09.021
- 756 López-Valverde, M. A. (2022). *IAA/CSIC temperature and co2 density profiles in mars*  
 757 *year 34 retrieved from the 1st year of nomad/tgo solar occultation observations*  
 758 [dataset]. Retrieved from <https://zenodo.org/record/7086187> doi:  
 759 10.5281/zenodo.7086187
- 760 López-Valverde, M. A., Gerard, J.-C., González-Galindo, F., Vandaele, A.-C., Thomas, I.,  
 761 Korablev, O., ... Rodríguez, J. (2018, Jan 10). Investigations of the mars upper  
 762 atmosphere with exomars trace gas orbiter. *Space Science Reviews*, *214*(1), 29.  
 763 Retrieved from <https://doi.org/10.1007/s11214-017-0463-4> (Como citar este  
 764 articulo: Lopez-Valverde, M.A., Gerard, JC., Gonzlez-Galindo, F. et al. Space Sci  
 765 Rev (2018) 214: 29. <https://doi.org/10.1007/s11214-017-0463-4> doi:  
 766 10.1007/s11214-017-0463-4
- 767 Mahieux, A., Vandaele, A., Robert, S., Wilquet, V., Drummond, R., Valverde, M. L., ...  
 768 Bertaux, J. (2015). Rotational temperatures of venus upper atmosphere as measured  
 769 by {SOIR} on board venus express. *Planet. Space Sci.*, *113-114*, 347 - 358. Retrieved

- 770 from <http://www.sciencedirect.com/science/article/pii/S0032063314004218>  
771 doi: 10.1016/j.pss.2014.12.020
- 772 Modak, A., Valverde, M.-A. L., Funke, B., Brines, A., Stolzenbach, A., Gonzalez-Galindo,  
773 F., et al. (2022). Retrieval of martian atmospheric vertical profiles from the first  
774 year of NOMAD/TGO solar occultation observations. *JGR-submitted*.
- 775 Montabone, L., Forget, F., Millour, E., Wilson, R., Lewis, S., Cantor, B., ... Wolff, M.  
776 (2015). Eight-year climatology of dust optical depth on mars. *Icarus*, 251, 65 - 95.  
777 Retrieved from  
778 <http://www.sciencedirect.com/science/article/pii/S0019103515000044>  
779 (Dynamic Mars) doi: <http://dx.doi.org/10.1016/j.icarus.2014.12.034>
- 780 Montabone, L., Spiga, A., Kass, D. M., Kleinboehl, A., Forget, F., & Millour, E. (2020).  
781 Martian year 34 column dust climatology from mars climate sounder observations:  
782 Reconstructed maps and model simulations. *Journal of Geophysical Research:*  
783 *Planets*, 125(8), e2019JE006111. doi: <https://doi.org/10.1029/2019JE006111>
- 784 Nakagawa, H., Jain, S. K., Schneider, N. M., Montmessin, F., Yelle, R. V., Jiang, F., ...  
785 Deighan, J. I. (2020). A warm layer in the nightside mesosphere of mars.  
786 *Geophysical Research Letters*, 47(4), e2019GL085646. Retrieved from  
787 <https://agupubs.onlinelibrary.wiley.com/doi/abs/10.1029/2019GL085646>  
788 (e2019GL085646 2019GL085646) doi: <https://doi.org/10.1029/2019GL085646>
- 789 Navarro, T., Forget, F., Millour, E., & Greybush, S. J. (2014). Detection of detached dust  
790 layers in the martian atmosphere from their thermal signature using assimilation.  
791 *Geophysical Research Letters*, 41(19), 6620–6626. Retrieved from  
792 <http://dx.doi.org/10.1002/2014GL061377> doi: 10.1002/2014GL061377
- 793 Neefs, E., Vandaele, A. C., Drummond, R., Thomas, I. R., Berkenbosch, S., Clairquin, R.,  
794 ... Jankowski, M. (2015, Oct). Nomad spectrometer on the exomars trace gas  
795 orbiter mission: part 1 & #x2014; design, manufacturing and testing of the infrared  
796 channels. *Appl. Opt.*, 54(28), 8494–8520. Retrieved from  
797 <http://ao.osa.org/abstract.cfm?URI=ao-54-28-8494> doi:  
798 10.1364/AO.54.008494
- 799 Robert, S., Vandaele, A., Thomas, I., Willame, Y., Daerden, F., Delanoye, S., ... the  
800 NOMAD team (2016). Expected performances of the nomad/exomars instrument.  
801 *Planetary and Space Science*, 124, 94 - 104. Retrieved from  
802 <http://www.sciencedirect.com/science/article/pii/S0032063315301203> doi:  
803 <http://dx.doi.org/10.1016/j.pss.2016.03.003>
- 804 Smith, M. D., Bougher, S. W., Encrenaz, T., Forget, F., & Kleinböhl, A. (2017). Thermal  
805 structure and composition. In R. M. Haberle, R. T. Clancy, F. Forget, M. D. Smith,  
806 & R. W. Zurek (Eds.), *The atmosphere and climate of mars* (p. 42-75). Cambridge  
807 University Press. doi: 10.1017/9781139060172.004
- 808 Starichenko, E. D., Belyaev, D. A., Medvedev, A. S., Fedorova, A. A., Korablev, O. I.,  
809 Trokhimovskiy, A., ... Hartogh, P. (2021). Gravity wave activity in the martian  
810 atmosphere at altitudes 20-160 km from acs/tgo occultation measurements. *Journal*  
811 *of Geophysical Research: Planets*, 126(8), e2021JE006899. Retrieved from  
812 <https://agupubs.onlinelibrary.wiley.com/doi/abs/10.1029/2021JE006899>  
813 (e2021JE006899 2021JE006899) doi: <https://doi.org/10.1029/2021JE006899>
- 814 Stiller, G. P. (Ed.). (2000). *The Karlsruhe Optimized and Precise Radiative Transfer*  
815 *Algorithm (KOPRA)* (Vol. FZKA 6487). Forschungszentrum Karlsruhe.
- 816 Thomas, I. R., Aoki, S., Trompet, L., Robert, S., Depiesse, C., Willame, Y., ... Bellucci,  
817 G. (2021). Calibration of nomad on esa's exomars trace gas orbiter: Part 1 ? the  
818 solar occultation channel. *Planetary and Space Science*, 105411. Retrieved from  
819 <https://www.sciencedirect.com/science/article/pii/S0032063321002506>  
820 doi: <https://doi.org/10.1016/j.pss.2021.105411>
- 821 Thomas, I. R., Vandaele, A. C., Robert, S., Neefs, E., Drummond, R., Daerden, F., ...  
822 Team, N. (2016, FEB 22). Optical and radiometric models of the NOMAD  
823 instrument part II: the infrared channels - SO and LNO [Article]. *OPTICS*  
824 *EXPRESS*, 24(4), 3790-3805. Retrieved from

- 825 <http://www.opticsexpress.org/abstract.cfm?URI=oe-24-4-3790> doi:  
826 {10.1364/OE.24.003790}
- 827 Trompet, L., Mahieux, A., Ristic, B., Robert, S., Wilquet, V., Thomas, I. R., ... Bertaux,  
828 J.-L. (2016, Nov). Improved algorithm for the transmittance estimation of spectra  
829 obtained with soir/venus express. *Appl. Opt.*, *55*(32), 9275–9281. Retrieved from  
830 <http://opg.optica.org/ao/abstract.cfm?URI=ao-55-32-9275> doi:  
831 10.1364/AO.55.009275
- 832 Trompet, L., Vandaele, A.-C., Thomas, I., Aoki, S., ..., F. D., & the NOMAD team.  
833 (2022). Carbon dioxide retrievals from nomad-so on esa's exomars trace gas orbiter  
834 and temperature profiles retrievals with the hydrostatic equilibrium equation. i.  
835 description of the method. *JGR-submitted*.
- 836 Vandaele, A. C., Korabiev, O., Daerden, F., Aoki, S., Thomas, I. R., Altieri, F., ... Team,  
837 A. S. (2019). Martian dust storm impact on atmospheric h<sub>2</sub>o and d/h observed by  
838 exomars trace gas orbiter. *Nature*, *568*(7753), 521-525. Retrieved from  
839 <https://doi.org/10.1038/s41586-019-1097-3> doi: 10.1038/s41586-019-1097-3
- 840 Vandaele, A. C., Lopez-Moreno, J.-J., Patel, M. R., Bellucci, G., Daerden, F., Ristic, B.,  
841 ... Wolff, M. (2018, 6). Nomad, an integrated suite of three spectrometers for the  
842 exomars trace gas mission: Technical description, science objectives and expected  
843 performance. *Space Science Reviews*, *214*(5), 80. Retrieved from  
844 <https://doi.org/10.1007/s11214-018-0517-2> doi: 10.1007/s11214-018-0517-2
- 845 Villanueva, G. L., Liuzzi, G., Aoki, S., Stone, S. W., Brines, A., Thomas, I. R., ...  
846 Vandaele, A. C. (2022). The deuterium isotopic ratio of water released from the  
847 martian caps as measured with tgo/nomad. *Geophysical Research Letters*, *49*(12),  
848 e2022GL098161. Retrieved from  
849 <https://agupubs.onlinelibrary.wiley.com/doi/abs/10.1029/2022GL098161>  
850 (e2022GL098161 2022GL098161) doi: <https://doi.org/10.1029/2022GL098161>
- 851 von Clarmann, T., Glatthor, N., Grabowski, U., Höpfner, M., Kellmann, S., Kiefer, M., ...  
852 López-Puertas, M. (2003). Retrieval of temperature and tangent altitude pointing  
853 from limb emission spectra recorded from space by the Michelson Interferometer for  
854 Passive Atmospheric Sounding (MIPAS). *J. Geophys. Res.*, *108*(D23). doi:  
855 10.1029/2003JD003602
- 856 Wolff, M., López-Valverde, M. A., Madeleine, J.-B., J., W. R., M., S., Foucher, F., &  
857 Delory, G. (2017). Chapter 6 - radiative processes: Techniques and applications. In  
858 B. Haberle, M. Smith, T. Clancy, F. Forget., & R. Zurek (Eds.), *The atmosphere and*  
859 *climate of mars* (p. 106-171). Cambridge University Press. Retrieved from  
860 [www.cambridge.org/9781107016187](http://www.cambridge.org/9781107016187) doi: 10.1017/9781139060172

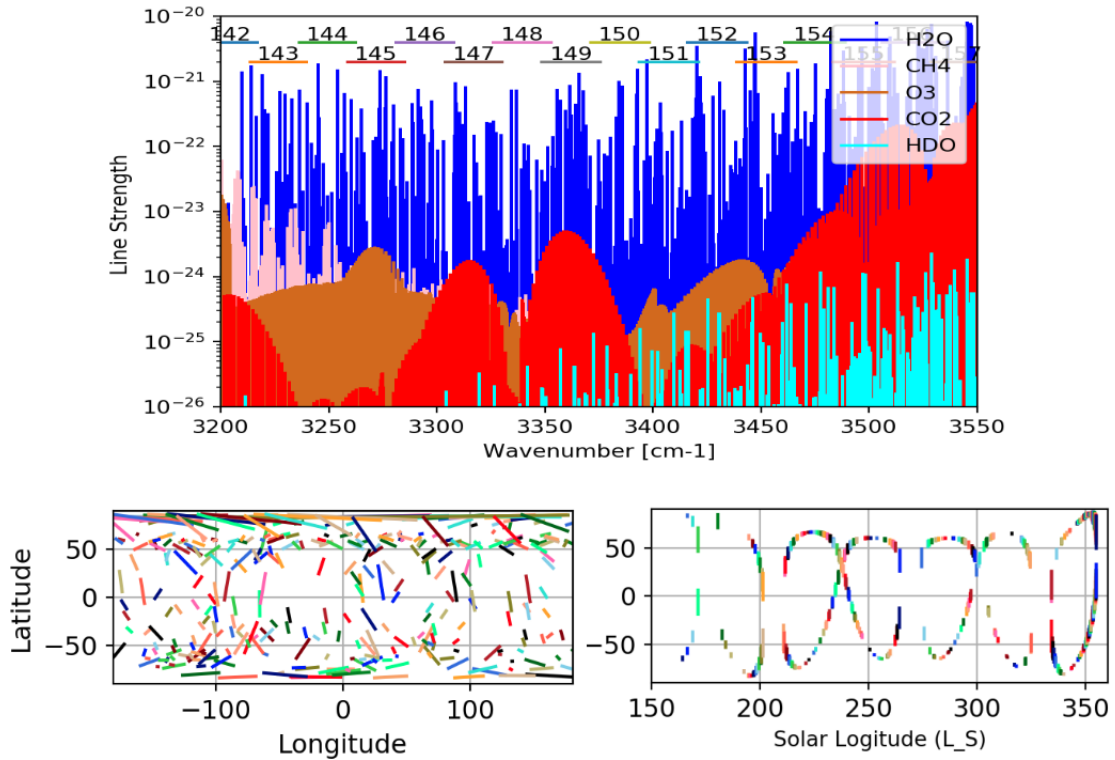


**Figure 1.** Top panel: Spectral location of NOMAD/SO diffraction order 149, and other adjacent orders, with indication of the strongest ro-vibrational absorption lines by some atmospheric species (positions and line strengths from Hitran2016). Bottom panels: latitude, longitude and solar longitude of the about 350 scans with solar occultation measurements in order 149 during the 1st year of NOMAD operations. Colors in the bottom panels are arbitrary, used for clarity.

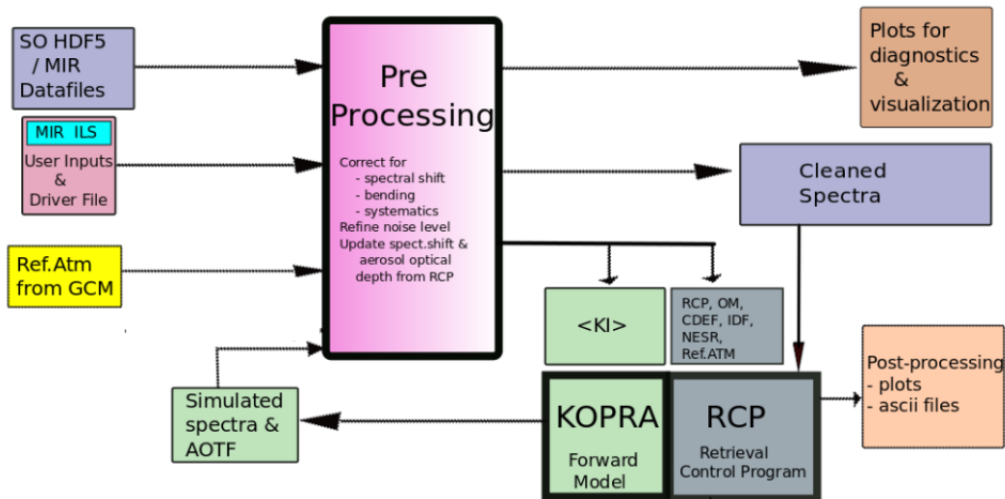


**Figure 2.** Pipeline of the NOMAD and ACS data analysis at IAA. The preprocessing block performs cleaning of residual spectral shifts and bendings, characterization of the ILS from the observed spectra, in addition to auxiliary plots and splitting of the spectra in spectral micro-windows before the inversion is performed by KOPRA and RCP. See text for details.

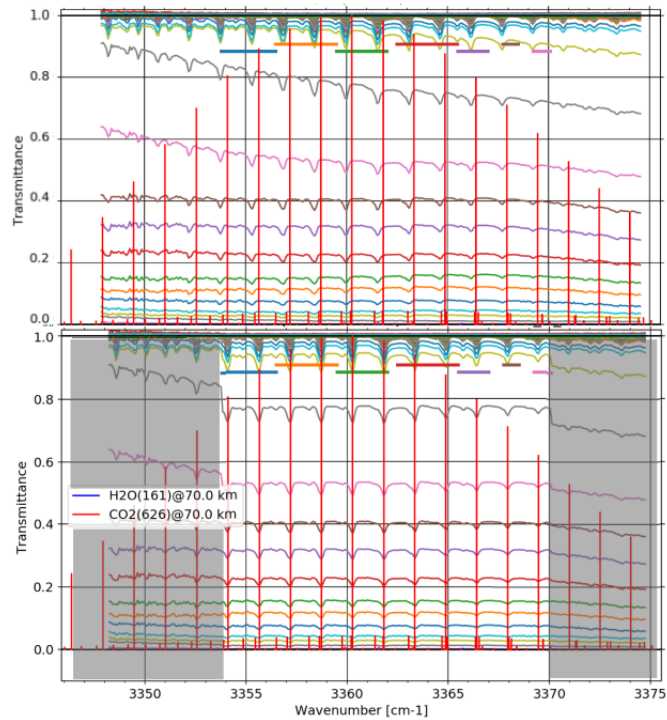


**Figure 3.** Example of our cleaning method applied to diffraction order 149 in one specific scan (20180423\_204351\_1p0a\_SO\_A\_I). Top panel, all the original spectra (calibrated transmittances) taken in this scan, showing clear bending effects and spectral shifts. Bottom panel, spectra after cleaning. Notice the cleaning is only applied to a subset of the full diffraction order (the rest is shaded in grey in the bottom panel). Vertical red solid lines indicate the expected position of the CO<sub>2</sub> spectral lines (Hitran2016). The seven short horizontal lines in different colors near the top of the panels indicate the micro-windows used in this order (see text for details).

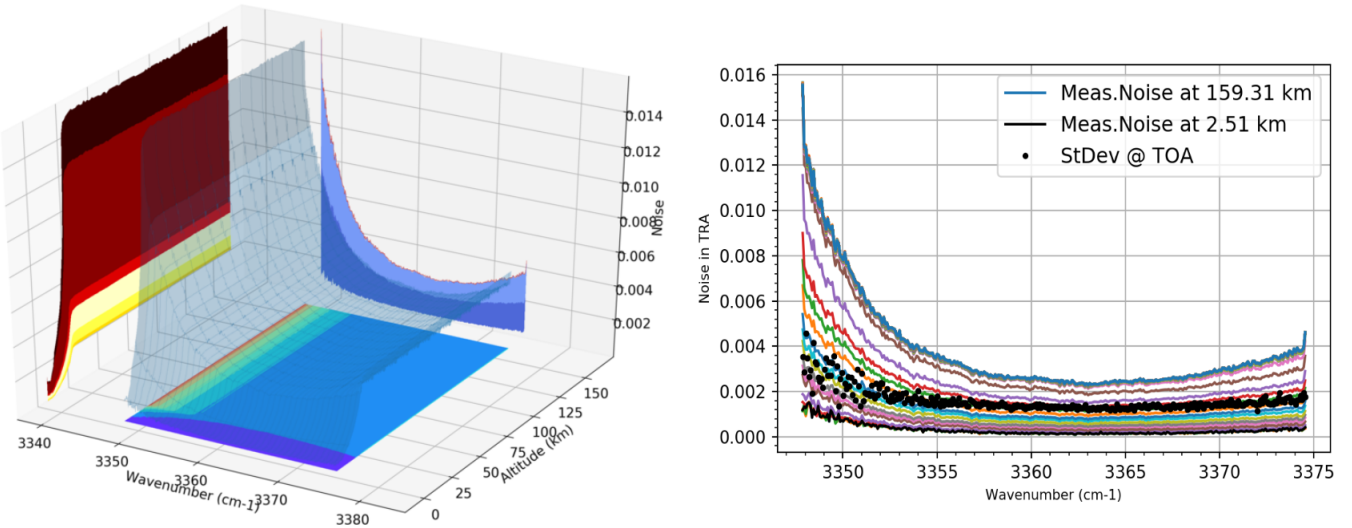


**Figure 4.** Measurement noise in transmittance in the order 149 of scan *20180423\_204351\_1p0a\_SO\_A\_I*, typical of all scans in this diffraction order. Left panel, variations in the spectral and altitude dimensions. Right-hand panel: alternative view of the projection onto the wavenumber-noise plane to appreciate the quasi-random variations; each line represents a noise spectrum (at one tangent altitude). The black-dots are the standard deviation of transmittance vertical profiles near the top of the atmosphere. The color scales in both panels are arbitrary. See text for details.

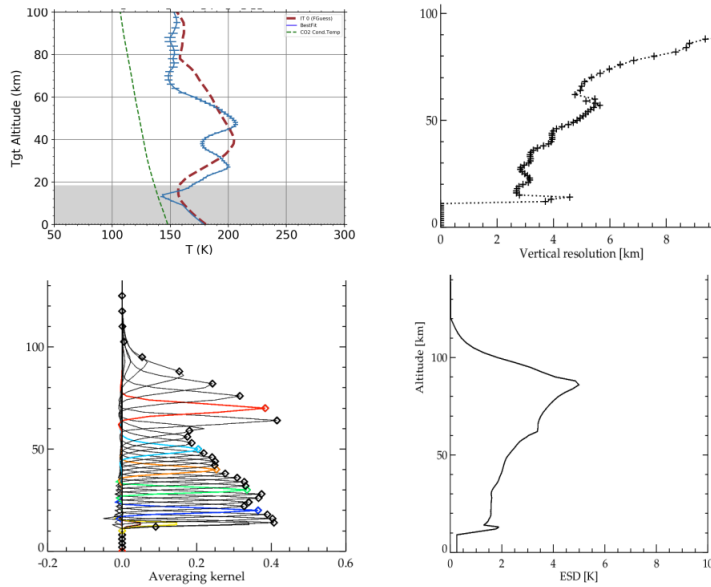


**Figure 5.** Retrieved temperature profile from scan *20180423\_204351\_1p0a\_SO\_A\_I* with error bars (top-left panel), where the red dashed line is the *a priori* profiles, and the green dashed line is the CO<sub>2</sub> condensation temperature, added for reference. Bottom-left: rows of the Averaging Kernel matrix selected at some altitudes. Bottom-right: retrieval error in the Temperature profile. Top-right: Vertical resolution, as given by the widths of the averaging kernel rows.

Accepted Article

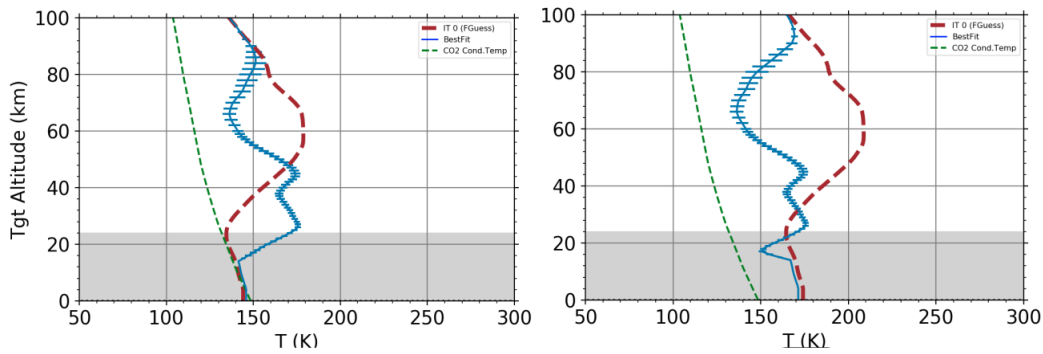


**Figure 6.** Effect of the *a priori* temperature on the retrieval for scan *20180423\_204351\_1p0a\_SO-A-I*. Left panel: inversion using the nominal *a priori* temperature profile. Right panel: using the *a priori* increased by 30 K.

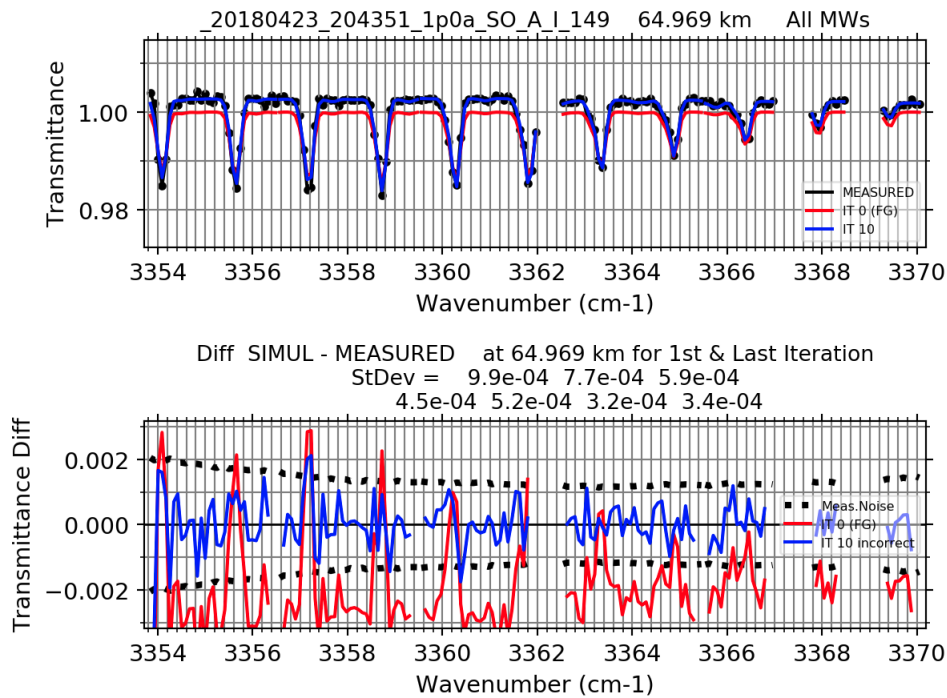


**Figure 7.** Best fit spectrum to the NOMAD cleaned transmittances from scan *20180423\_204351\_1p0a\_SO-A-I* at a tangent altitude of about 65 km. The top panel shows the measured spectrum in solid black line with dots, the best fit spectrum at the end of the inversion in blue, and the spectrum obtained with the *a priori* atmospheric profile in red. The spectrum is split in 7 segments which correspond to the 7 micro-windows used in the inversion (see text). The lower panel shows the residuals (Model fit - NOMAD) in blue, together with the same magnitude but with the model spectrum for the *a priori* atmosphere, in red. The dotted lines represent the NOMAD/SO measurement error used in the inversion.

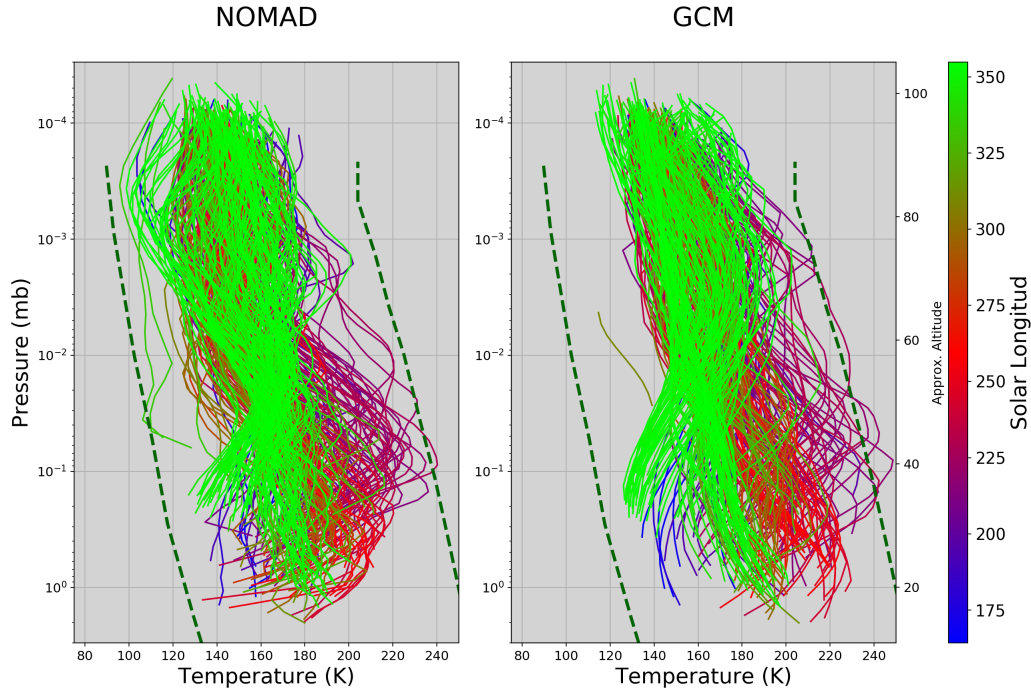


**Figure 8.** Envelope of all the retrieved temperature profiles (left-hand panel) compared to the *a priori* data, from the LMD-MGCM (right-hand panel). The colors in each scan indicate the Solar Longitude. The thick dashed lines represent the extreme temperatures at any time and place on Mars, after Smith et al. (2017). Approximate altitudes added as a quick guide.

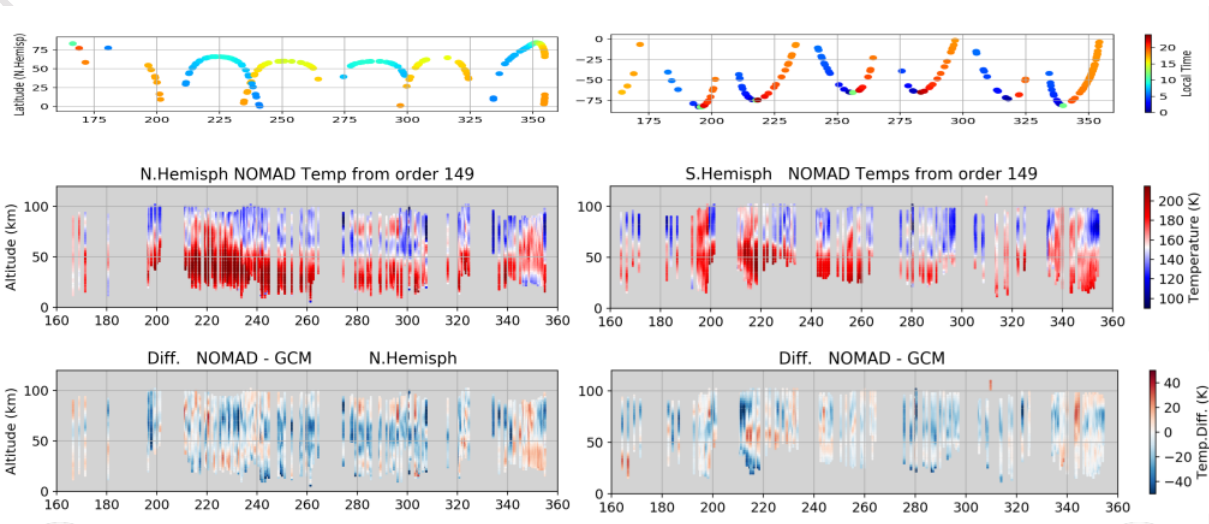


**Figure 9.** Distribution of all the retrieved temperatures with latitude and solar time throughout MY34, split in the two hemispheres (NH in the left hand side panels and SH in the right hand side panels). The top panels show the latitudes and the Local Solar Time of the observations. The center panels show the temperatures, and the lower panels the difference between the NOMAD retrievals and the GCM (*a priori*).



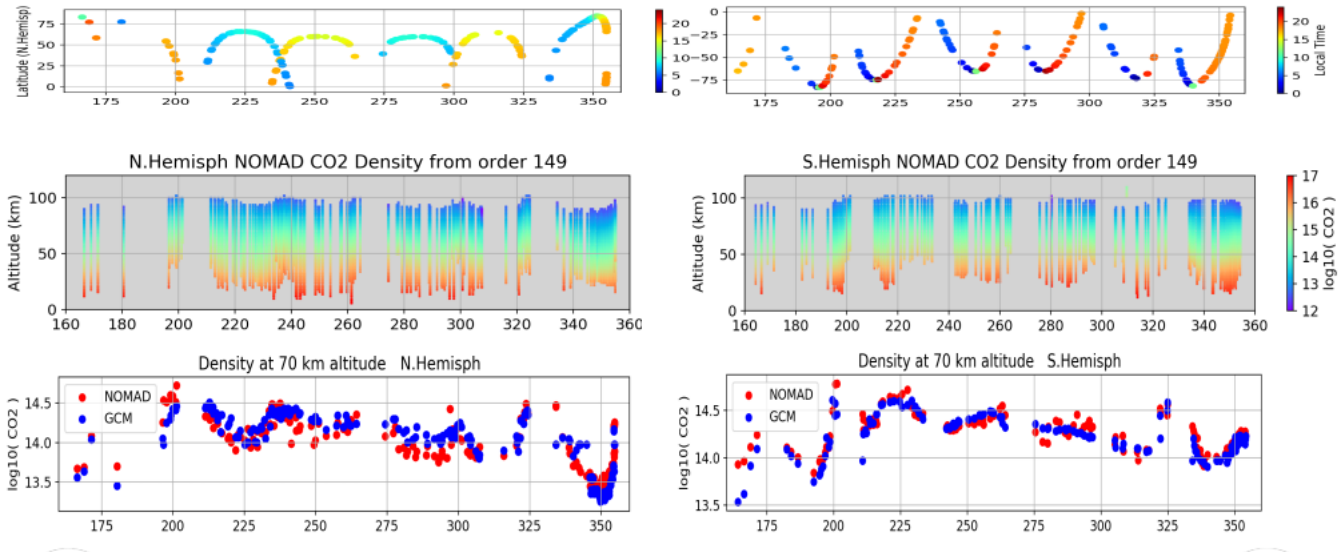


**Figure 10.** Global distribution of the retrieved CO<sub>2</sub> densities for MY34, split in the two hemispheres (NH in panels on the left and SH on the right). The top panels show the latitudes and the Local Solar Time of the observations and the central panels show the densities in log scale. The bottom panels show the density variation at 70 km altitude through the mission, including latitudinal and seasonal variations (see text); red dots: NOMAD densities, blue dots: GCM data.

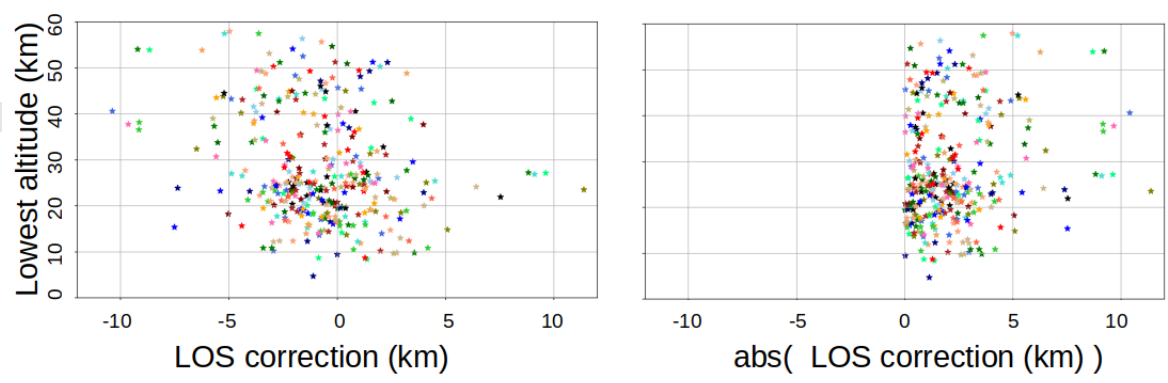


**Figure 11.** Distribution of the retrieved LOS correction with altitude of all the retrieved profiles (left panel) and the same but in absolute values (right panel). See text for details.

Accepted Article

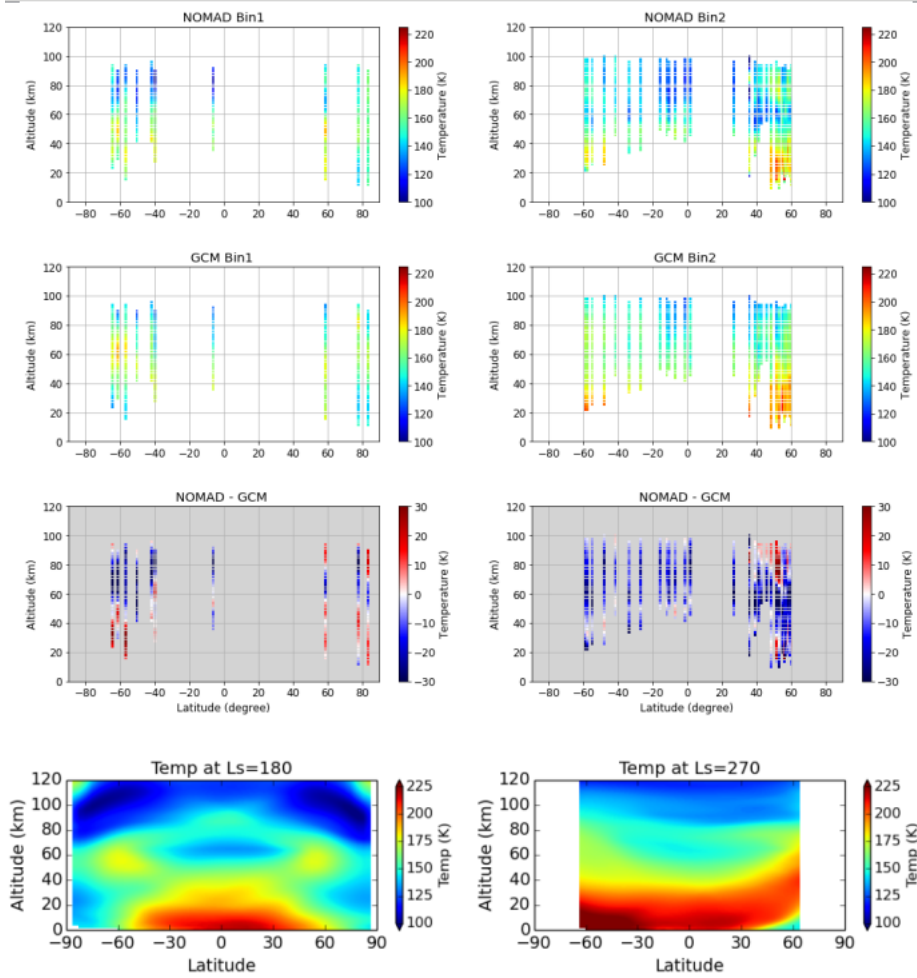


**Figure 12.** Latitudinal distribution of the retrieved NOMAD temperatures in two seasonal periods. Left panels: period  $L_s=160^\circ\text{--}190^\circ$ ; right-hand side: period  $L_s=285^\circ\text{--}305^\circ$ . Top panels: NOMAD retrieved temperatures; 2nd from top: GCM temperatures at the same locations and local times; 3rd panels from top: difference NOMAD-GCM; and bottom panels: altitude/latitude cross sections of the LMD-MGCM temperatures at  $L_s 180^\circ$  and  $270^\circ$ , for comparison.

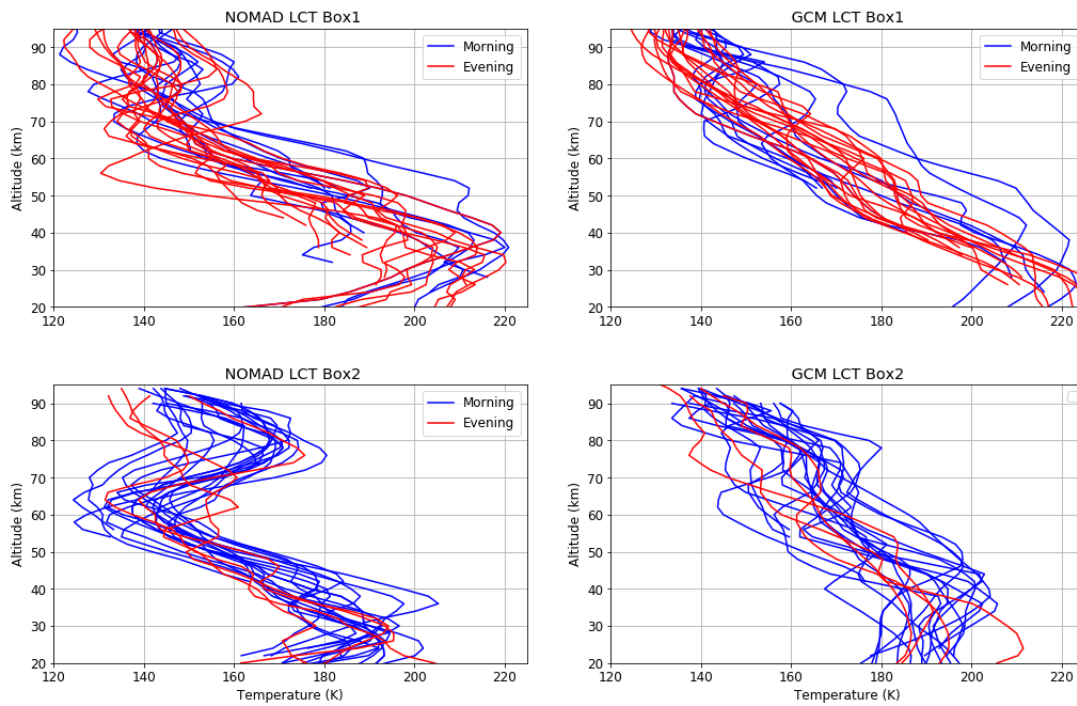


**Figure 13.** Local Time variations in 2 specific periods and locations, selected to minimize latitudinal and seasonal effects. Top panels: CT Box 1, defined by Latitudes  $20^{\circ}\text{N}$ - $50^{\circ}\text{N}$  and Ls  $230^{\circ}$ - $250^{\circ}$ . Bottom panes: CT Box 2, defined by Latitudes  $30^{\circ}\text{N}$ - $60^{\circ}\text{N}$  and Ls  $290^{\circ}$ - $310^{\circ}$ . See text for details.

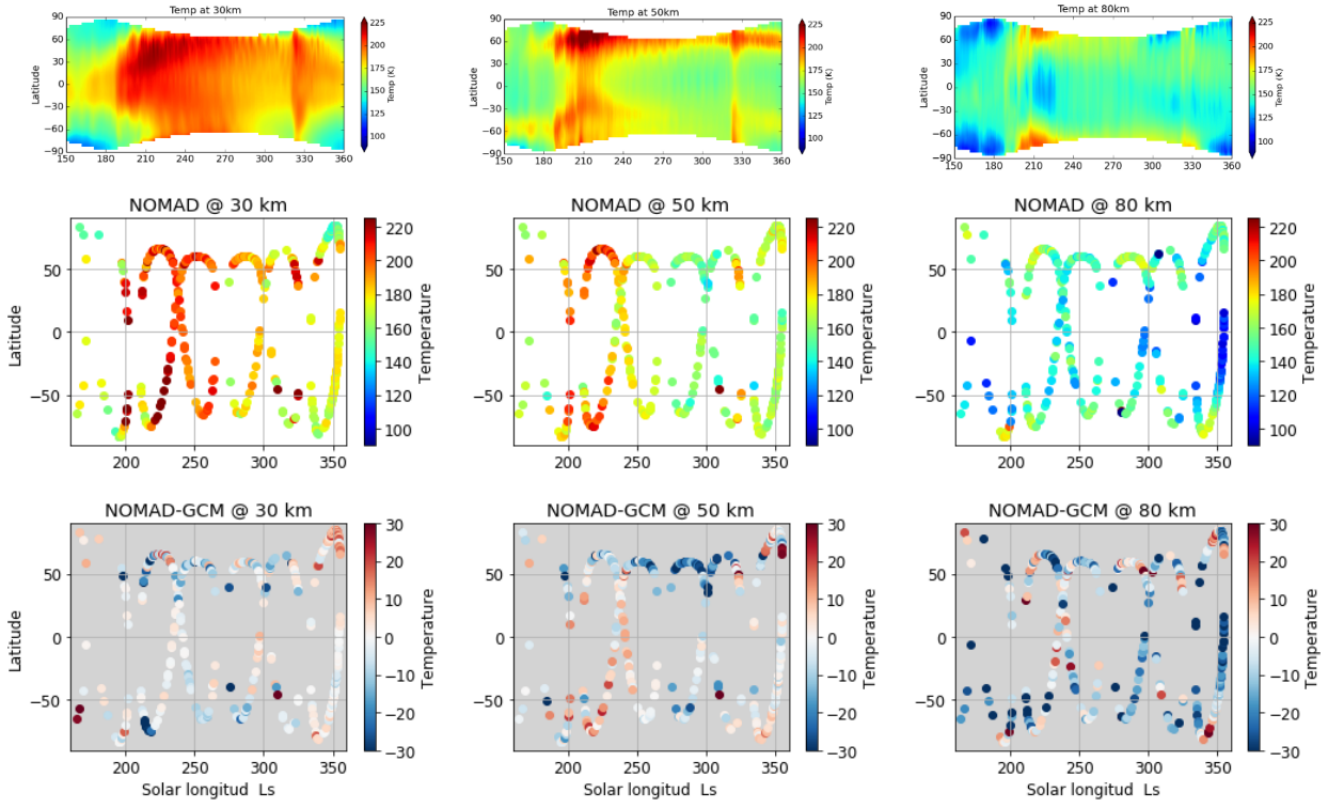


**Figure 14.** Temperature latitude-solar longitude cross sections at 3 different altitudes, 30 km (left panels), 50 km (central column's panels) and 80 km (right-hand panels). The retrieved temperatures are shown in the central row, while Latitude-Ls cross sections from the LMD-MGCM are shown in the top panel, for reference. See text for details.

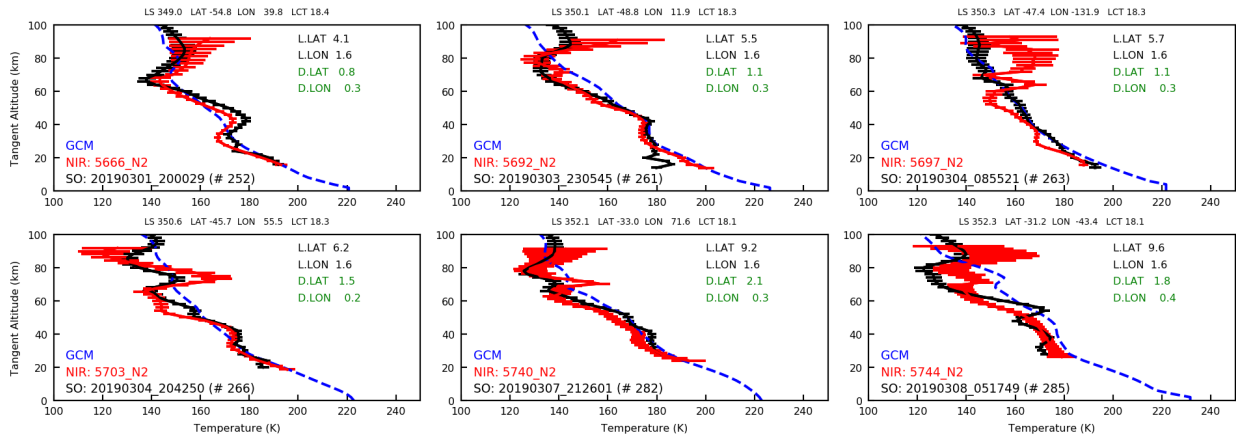


**Figure 15.** Comparison between NOMAD/SO and ACS/NIR temperature profiles in the 6 closest coincidences, each of them in a separate panel. The panels titles indicate the locations of the profiles in latitude, longitude, local time and solar longitude. The NOMAD/SO temperature profile and error bars are in black, the ACS/NIR in red, and the GCM a priori in blue. Each instrument's orbit number identifier is also included for easy reference; in the case of NOMAD/SO we also added a number in bracket for internal reference. L.LAT and L.LON indicate the extension of the NOMAD/SO profile in latitude and longitude (in degree), respectively. D.LAT and D.LON indicate the separation between the NOMAD/SO and ACS/NIR profiles in latitude and longitude respectively. See text for details.

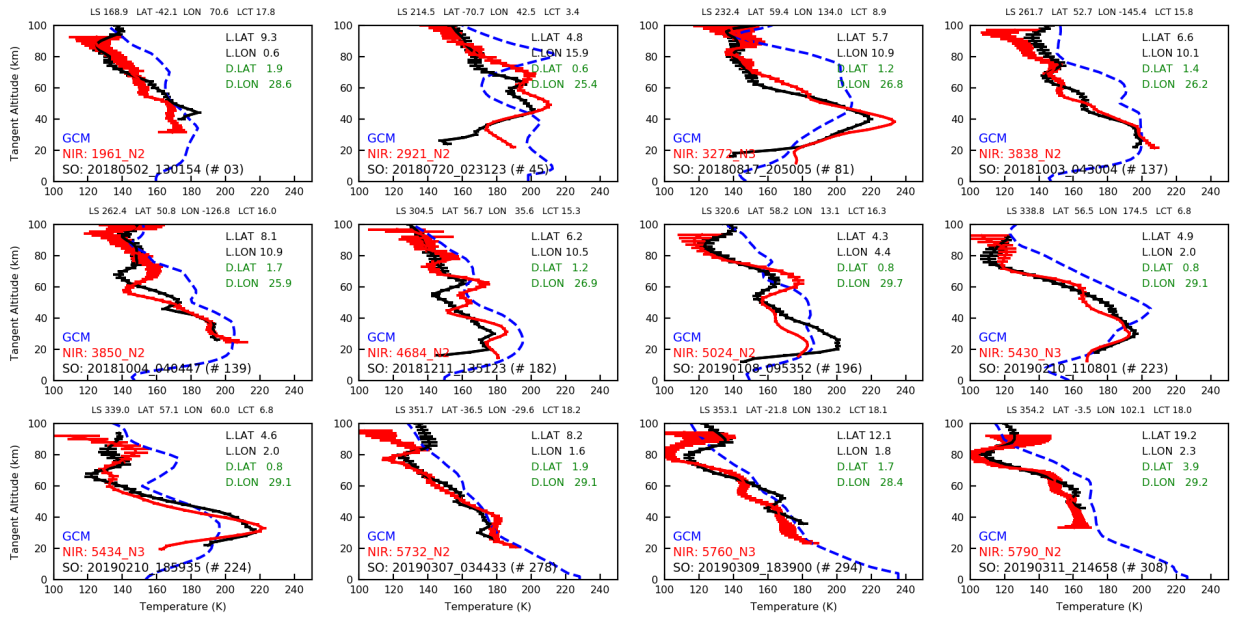


**Figure 16.** Similar to Figure 15 but for a selection of 12 NOMAD/SO and ACS/NIR profiles which show a good agreement between them and significant differences with the GCM *a priori* profile. See text for details.

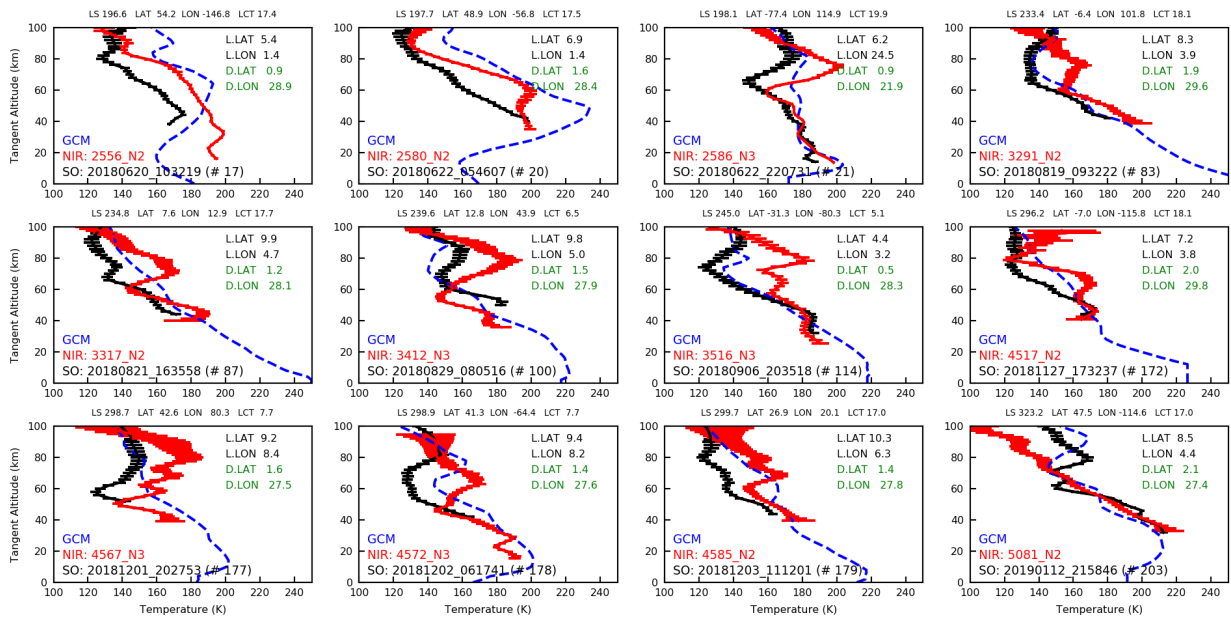


**Figure 17.** Similar to Figure 15 but for the 12 NOMAD/SO and ACS/NIR profiles with the largest differences. See text for details.

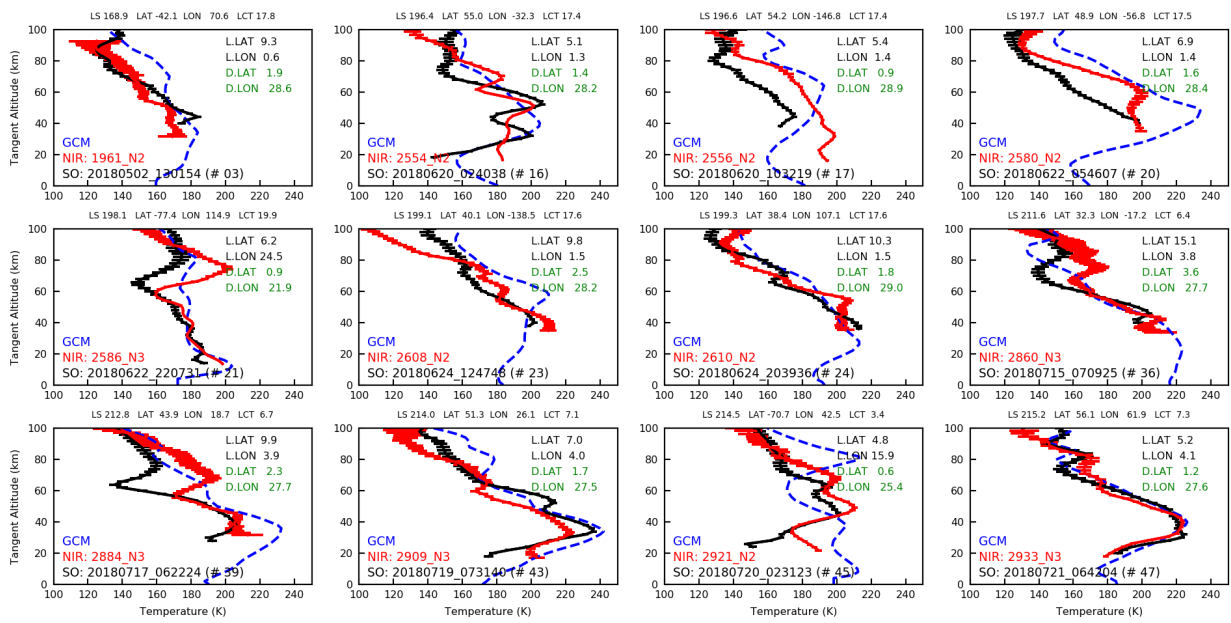


**Figure A1.** First dozen of NOMAD/SO and ACS/NIR collocated profiles from the set of 95 coincidences mentioned in the text. Figure format similar to Figure 15.



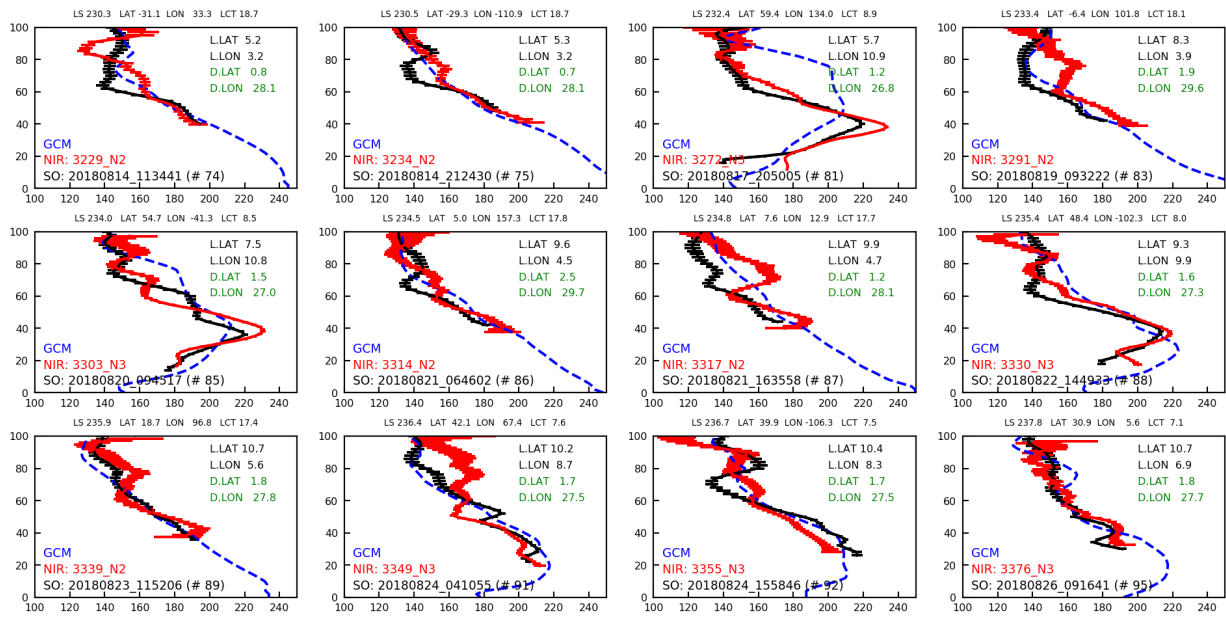
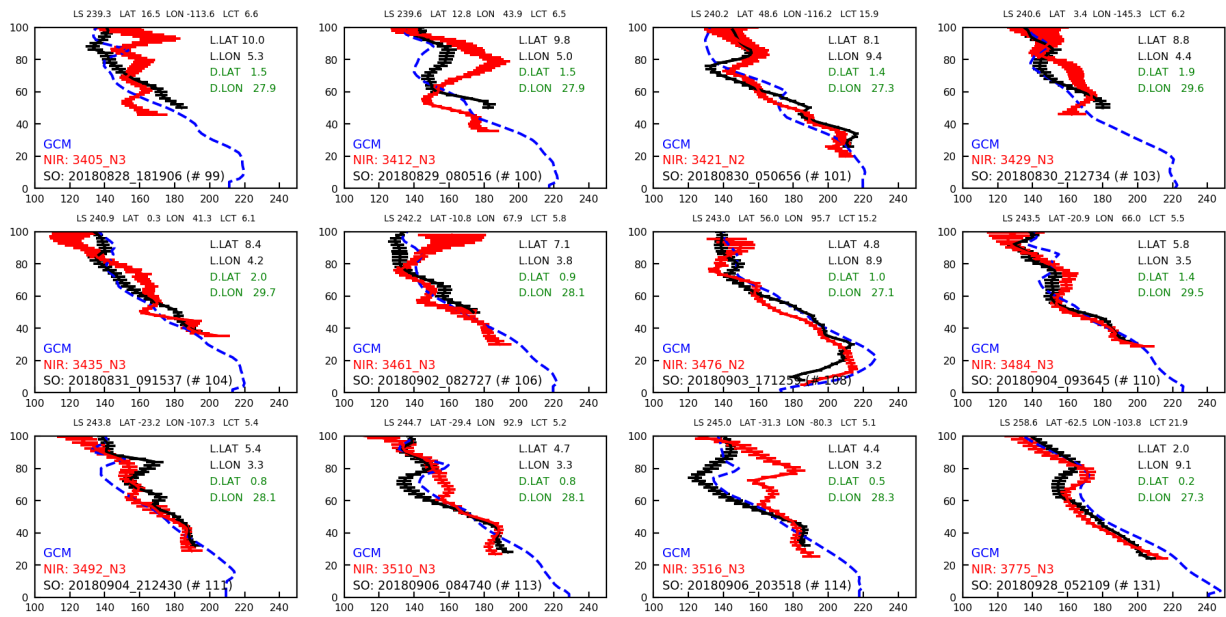


Figure A2. As Figure A1 but for the 2nd dozen of profiles.



**Figure A3.** As Figure A1 but for the 3rd dozen of profiles.

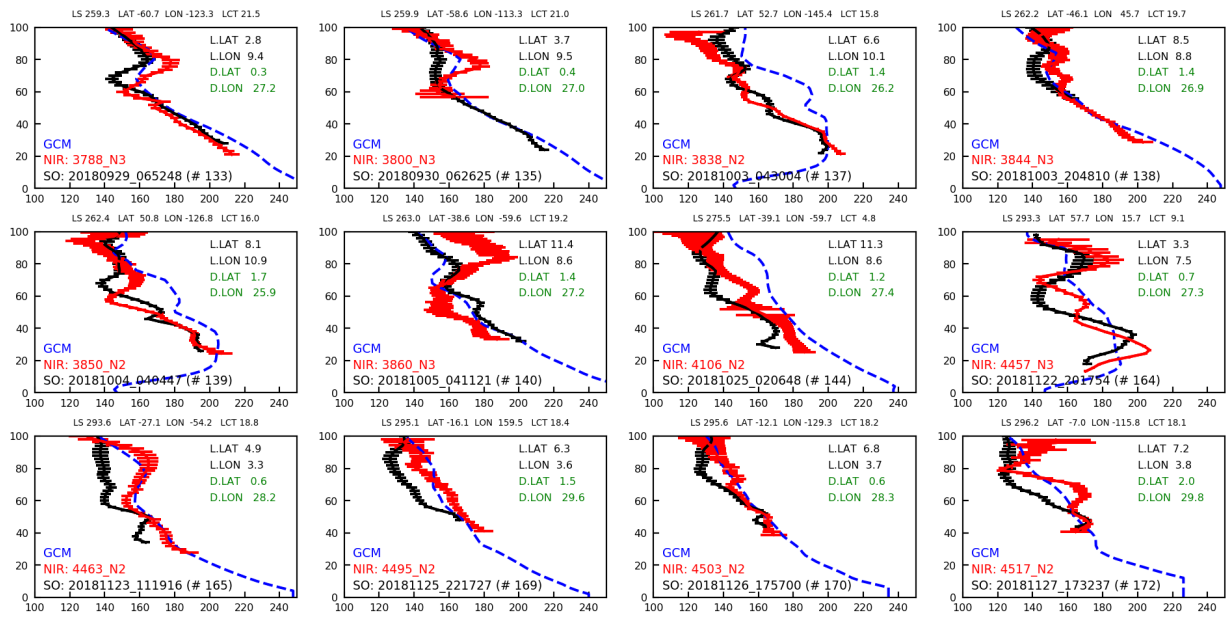


Figure A4. As Figure A1 but for the 4th dozen of profiles.

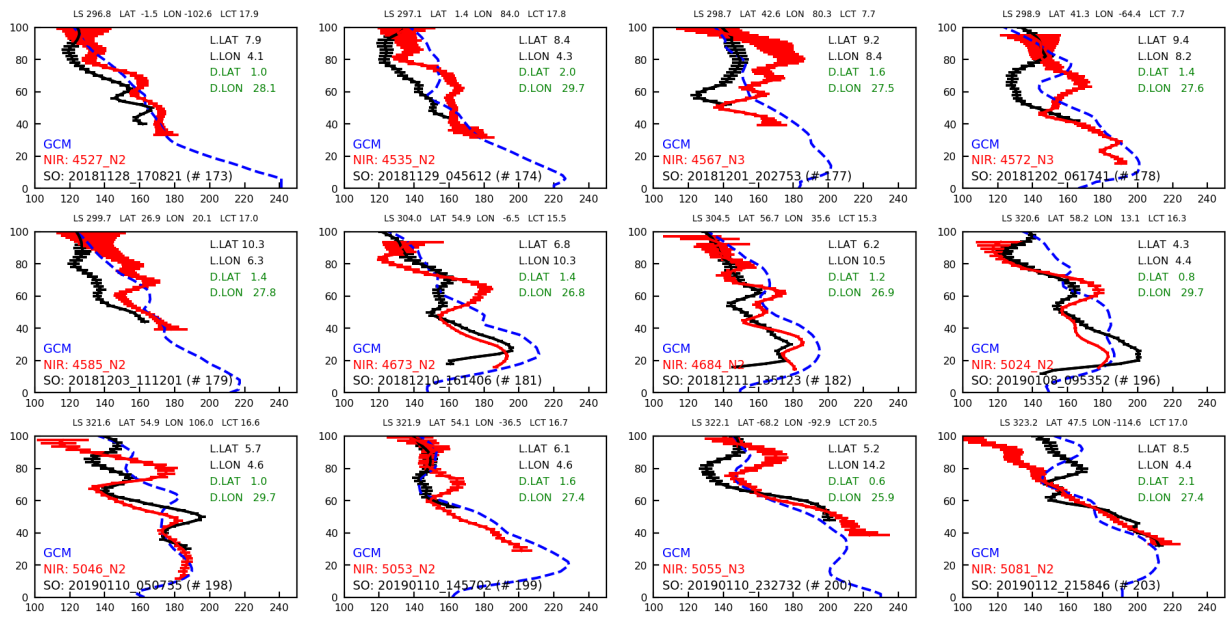


Figure A5. As Figure A1 but for the 5th dozen of profiles.

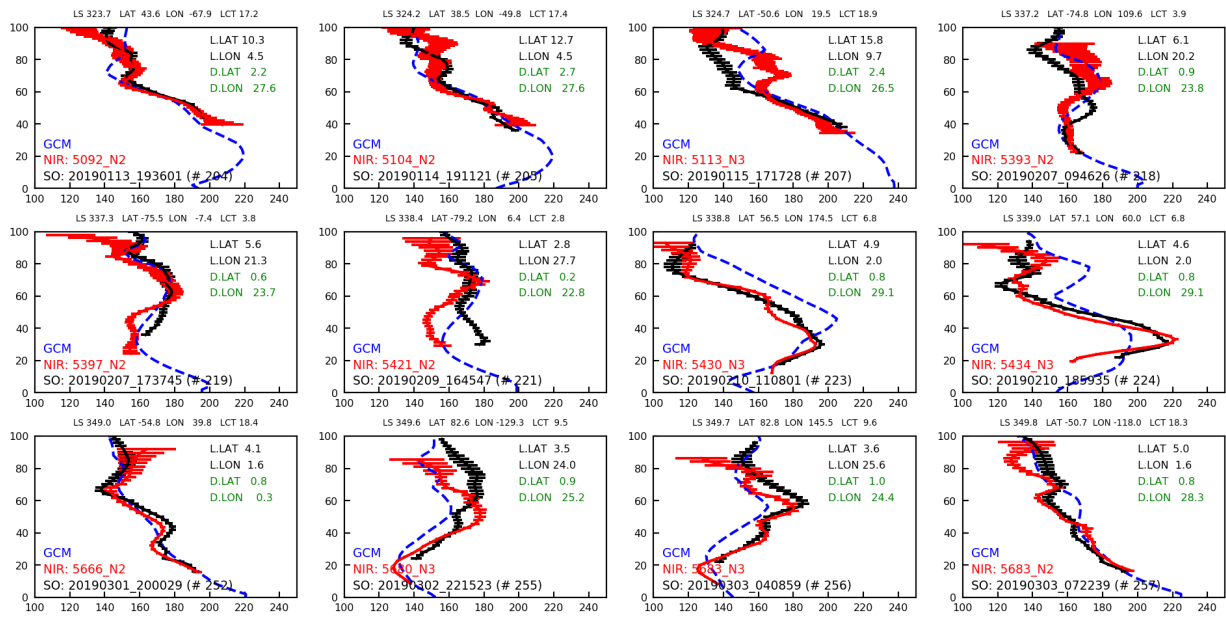


Figure A6. As Figure A1 but for the 6th dozen of profiles.

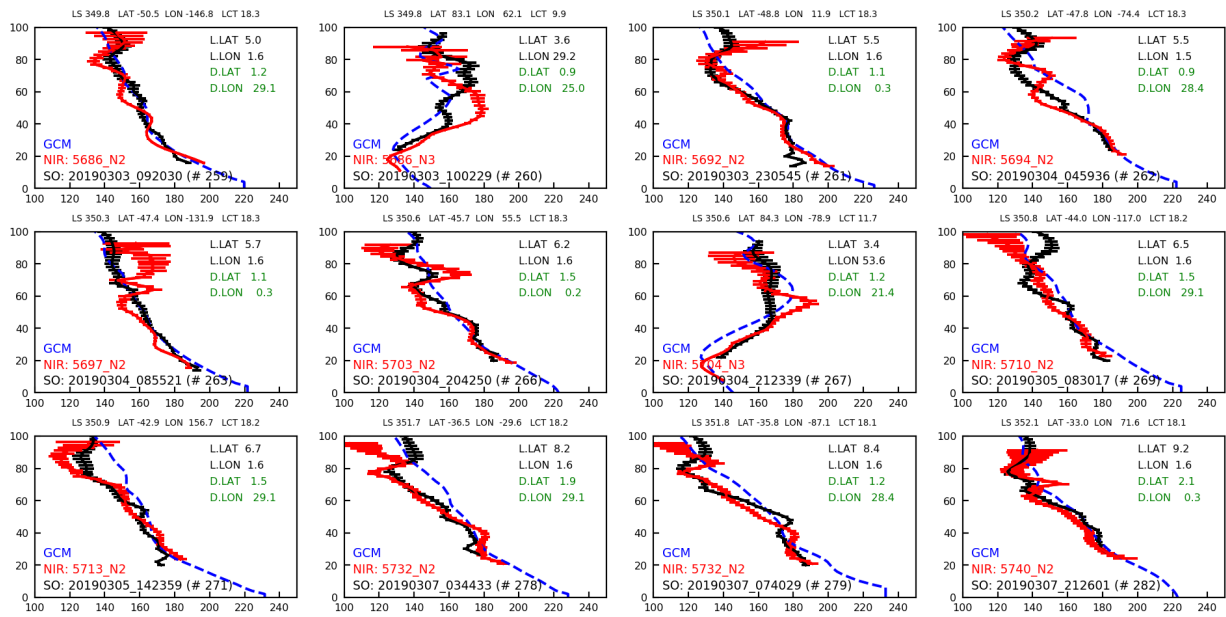


Figure A7. As Figure A1 but for the 7th dozen of profiles.

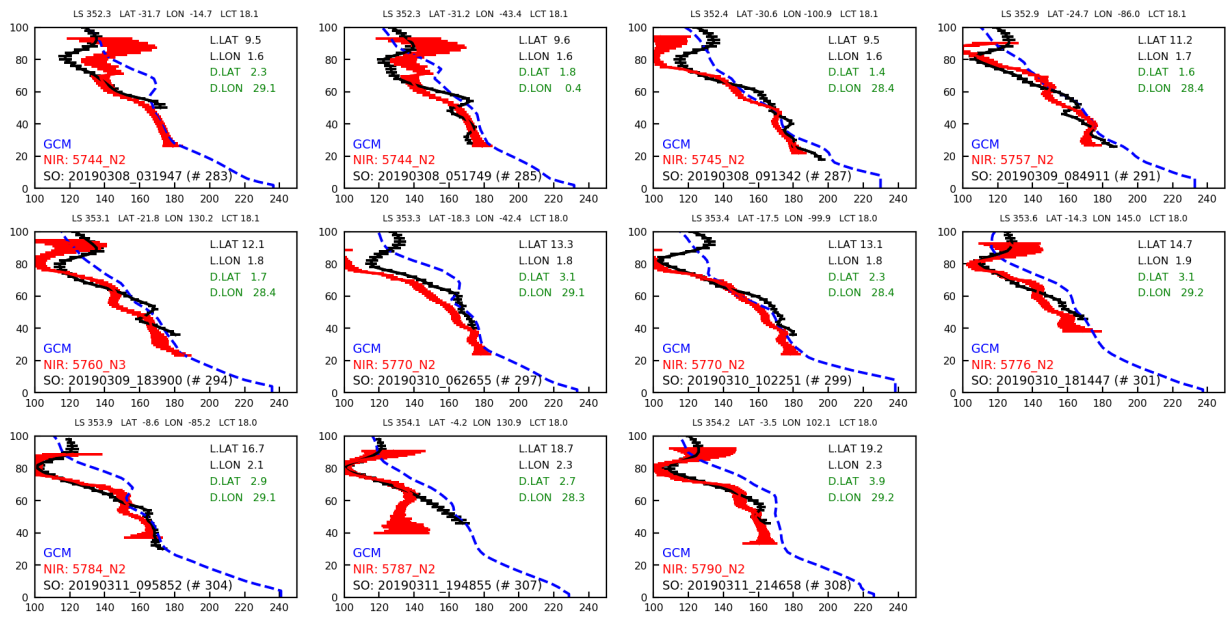


Figure A8. As Figure A1 but for the 8th dozen of profiles.